Storm-Scale Data Assimilation and Ensemble Forecasts for the 27 April 2011 Severe Weather Outbreak in Alabama

NUSRAT YUSSOUF

Cooperative Institute for Mesoscale Meteorological Studies, University of Oklahoma, and NOAA/OAR/National Severe Storms Laboratory, Norman, Oklahoma

DAVID C. DOWELL

NOAA/OAR/Earth System Research Laboratory, Boulder, Colorado

LOUIS J. WICKER

NOAA/OAR/National Severe Storms Laboratory, Norman, Oklahoma

KENT H. KNOPFMEIER AND DUSTAN M. WHEATLEY

Cooperative Institute for Mesoscale Meteorological Studies, University of Oklahoma, and NOAA/OAR/National Severe Storms Laboratory, Norman, Oklahoma

(Manuscript received 19 August 2014, in final form 24 March 2015)

ABSTRACT

As part of NOAA's Warn-on-Forecast (WoF) initiative, a multiscale ensemble-based assimilation and prediction system is developed using the WRF-ARW model and DART assimilation software. To evaluate the capabilities of the system, retrospective short-range probabilistic storm-scale (convection allowing) ensemble analyses and forecasts are produced for the 27 April 2011 Alabama severe weather outbreak. Results indicate that the storm-scale ensembles are able to analyze the observed storms with strong low-level rotation at approximately the correct locations and to retain the supercell structures during the 0–1-h forecasts with reasonable accuracy. The system predicts the low-level mesocyclones of significant isolated tornadic supercells that align well with the locations of radar-derived rotation. For cases with multiple interacting storms in close proximity, the system tends to produce more variability in mesocyclone forecasts from one initialization time to the next until the observations show the dominance of one of the cells. The short-range ensemble probabilistic forecasts obtained from this continuous 5-min storm-scale 6-h-long update system demonstrate the potential of a frequently updated, high-resolution NWP system that could be used to extend severe weather warning lead times. This study also demonstrates the challenges associated with developing a WoF-type system. The results motivate future work to reduce model errors associated with storm motion and spurious cells, and to design storm-scale ensembles that better represent typical 1-h forecast errors.

1. Introduction

The National Oceanic and Atmospheric Administration's (NOAA) Warn-on-Forecast (WoF; Stensrud et al. 2009a) research and development project envisions incorporating numerical weather prediction (NWP) model forecasts into the severe and hazardous weather warning decision-making process of NOAA's National Weather Service (NWS). The vision for a WoF system is a continuously updated, ensemble-based data assimilation and probabilistic forecast system that can provide quantitative information regarding the evolution of severe thunderstorm events on a 1-h time scale and potentially help operational forecasters improve tornado warning lead times. To achieve this goal, assimilation of Doppler radar and other available observations of ongoing convection in storm-scale NWP models is crucial (Stensrud et al. 2009a). Despite the current limitations and challenges of associated with the observations,

Corresponding author address: Dr. Nusrat Yussouf, NOAA/National Severe Storms Laboratory/National Weather Center, 120 David L. Boren Blvd., Norman, OK 73072.
E-mail: nusrat.yussouf@noaa.gov

DOI: 10.1175/MWR-D-14-00268.1

models, and assimilation methods, progress has been made over the past decade in assimilating radar observations from severe convective storms into storm-scale models (Stensrud et al. 2009a, 2013).

One data assimilation approach that shows promise for the envisioned WoF-type system is the ensemble Kalman filter (EnKF). Research during the past decade shows that good representation of ongoing convection can be achieved from storm-scale EnKF-based analyses within a homogeneous, single-sounding idealized framework (e.g., Snyder and Zhang 2003; Dowell et al. 2004; Tong and Xue 2005; Xue et al. 2006; Aksoy et al. 2009, 2010; Yussouf and Stensrud 2010, 2012; Dowell et al. 2011). To explore the efficacy of such a storm-scale ensemble-based EnKF framework for WoF-type application, Dawson et al. (2012) and Potvin and Wicker (2013) conducted idealized experiments and generated probabilistic forecasts of low-level rotation of supercell storms. In particular, Dawson et al. (2012) tested such a system for the 4–5 May 2007 Greensburg, Kansas, tornadic supercell case and show that short-range probabilistic forecasts of low-level rotation can be achieved with good accuracy from such a system. However, idealized experiments often use horizontally homogeneous and temporally constant environmental conditions and past studies illustrate that incorporating the influence of horizontal environmental variability and mesoscale forcing on the storm scale flows is very important for obtaining accurate predictions of tornadic supercell thunderstorms (Aksoy et al. 2009; Ziegler et al. 2010; Stensrud and Gao 2010).

The value of assimilating real radar observations into heterogeneous mesoscale environments has been examined in recent years and the results obtained are very encouraging (e.g., Dowell et al. 2010; Snook et al. 2011; Jung et al. 2012; Snook et al. 2012; Yussouf et al. 2013a; Putnam et al. 2014; Wheatley et al. 2014). For example, Snook et al. (2012) and Putnam et al. (2014) show that reasonable probabilistic forecasts of mesovortices within a mesoscale convective system can be achieved by using the Advanced Regional Prediction System (ARPS) model (Xue et al. 2000) and an EnKF system initialized from assimilating real observations within a realistic mesoscale environment. Yussouf et al. (2013a) investigated the benefits of assimilating real radar observations in a storm-scale data assimilation and forecast system using heterogeneous mesoscale environments for the 8 May 2003 Oklahoma City, Oklahoma, tornadic supercell storm and found that the ensemble system is able to predict the probability of a strong low-level vorticity track exceeding a threshold of $0.006\,s^{-1}$ for the tornadic supercell with good accuracy. The background storm environments used for that study are based on the same set of physics parameterization schemes (fixed physics) across the ensemble members. To quantify the impact of physics diversity within the ensemble on storm-scale forecasts, another recent study conducted by Yussouf et al. (2013b) used background storm environments from either fixed physics or multiphysics (Stensrud et al. 2000) mesoscale ensembles for the same tornadic supercell. Results show that the storm-scale ensemble with multiphysics background fields provides more realistic probabilistic forecasts of low-level rotation than that from the fixed-physics mesoscale background. All of these studies illustrate that reasonable short-range probabilistic forecasts of low-level rotation can be achieved for some supercell storms that are somewhat isolated in nature.

Whereas previous storm-scale data-assimilation and NWP studies have tended to focus on isolated convective storms or systems, more typical storm situations involve multiple interacting storms. Furthermore, tornadoes can form within a wide variety of parent storm modes ranging from discrete supercells and quasi-linear and mesoscale convective systems to tropical cyclones (Thompson et al. 2012; Edwards et al. 2012). Therefore, it is important to test storm-scale NWP systems for robustness in complicated situations with numerous supercell storms and storm interactions such as these.

One extreme tornado outbreak in recent years that caused severe damage across the southeastern part of the United States is the event from 27 April 2011. This event is unique in terms of the number of strong to violent tornadoes produced (199 total over the 24-h period) across 14 states, the number of resulting fatalities (316) and injuries (more than 2700), and the amount of damage (insurable loss exceeding $4 billion dollars) (Knupp et al. 2014). It is one of the most significant severe weather outbreaks in recent U.S. history. Of the 316 deaths reported, 313 are associated with the super outbreak of tornadoes during the afternoon and evening hours (NOAA 2012; TRAC 2012) of 27 April. In this study, we further investigate the utility of a multiscale ensemble data assimilation and forecast system for 0–1-h forecasts for the 27 April 2011 tornado outbreak, focusing specifically on northern Alabama. A 36-member multiphysics mesoscale and storm-scale data-assimilation and prediction system is developed. The mesoscale ensemble is used to provide the boundary conditions for a one-way-nested storm-scale ensemble centered on northern Alabama. Conventional observations are assimilated by the multiscale ensemble every hour to obtain realistic mesoscale environments. Before the onset of the Alabama tornado outbreak, data from four radars and conventional observations are assimilated into the storm-scale domain continuously every 5 min for a 6-h

period and these analyses are used to initialize frequent 1-h ensemble forecasts. Many of the supercell thunderstorms that passed through northern and central Alabama during the afternoon and evening hours on that day were long-lived supercells that produced long-track violent tornadoes, making this case an ideal candidate to demonstrate the capabilities of a WoF multiscale ensemble data assimilation and forecast system.

A brief overview of the 27 April severe weather outbreak in Alabama is provided in section 2, followed by the experiment design of both the multiscale and storm-scale radar data assimilation systems in section 3. Section 4 assesses the qualitative results of the analyses and frequent ensemble forecasts from the storm-scale 5-min analysis system. A final discussion is found in section 5.

2. Overview of the 27 April 2011 Alabama tornado outbreak

The 27 April 2011 tornado outbreak in Alabama was the most violent round of severe weather from the record-breaking 4-day-long (25–28 April) episode of significant severe weather that impacted the southern plains and southeastern United States. The severe weather on 27 April 2011 can be classified into three distinct events: an extensive early morning quasi-linear convective system (QLCS), a shorter midday QLCS over northern Alabama, and the widespread long-lived tornadic supercell outbreak during the afternoon and evening hours (Knupp et al. 2014). The focus of this data-assimilation and forecast study is on the super outbreak of tornadoes during the afternoon and evening hours over north and central Alabama.

An overview of environmental conditions and convective storm evolution is provided by Knupp et al. (2014) and NOAA (2012). By 1900 UTC 27 April 2011, thunderstorms had formed along two main lines in Mississippi and in scattered locations farther east into northern Alabama (Fig. 1a). At around 1930 UTC, a violent round of severe weather began over Alabama and lasted until midnight. Numerous supercell thunderstorms (Fig. 1b) went over much of northern and central Alabama, producing strong to violent tornadoes during this period (Fig. 1c). A list of the significant tornadoes that were rated as category 3 or higher on the enhanced Fujita (EF) scale is presented in Table 1. The Hackleburg–Phil Campbell–Tanner (referred to as the Hackleburg tornado from hereafter) tornado over northern Alabama exhibited the longest path, about 212 km, followed by another long-track tornado in Cordova that was approximately 200 km in length. The Tuscaloosa–Birmingham tornado caused the highest number of fatalities and injured more than 1000 people. Multiple operational Weather Surveillance Radar-1988 Dopplers (WSR-88Ds) documented the life cycle of these tornado outbreaks. These radars provide a unique dataset in which continuous 5-min storm-scale data-assimilation experiments are conducted to assess the capability of the system to forecast low-level rotation.

3. Experiment design

a. Multiscale WRF ensemble system

An ensemble-based multiscale data-assimilation and prediction system is designed using version 3.4.1 of the Advanced Research core of the Weather Research and Forecasting Model (WRF-ARW; Skamarock et al. 2008). The parent mesoscale model domain (Fig. 2a) covers the contiguous United States (CONUS) with a horizontal grid spacing of 15 km, and a storm-scale domain nested within the mesoscale domain covers northern Alabama and surroundings (Fig. 2b). A grid spacing of 3 km is used for the storm-scale domain, which is sufficient to produce storms with mesocyclones but is not capable of producing sub-mesocyclone-scale circulations such as tornadoes (Yussouf et al. 2013b). Both domains have 51 vertical grid levels, from the surface to 10 hPa aloft. A 36-member multiscale ensemble is initialized at 0000 UTC 27 April 2011 using the analyses from National Centers for Environmental Prediction's (NCEP) 21-member Global Ensemble Forecast System (GEFS; Toth et al. 2004; Wei et al. 2008). Out of the 21 members, the first 18 members are used to create a 36-member multiscale ensemble system. In addition, the first 18 members of the GEFS system provide the lateral boundary conditions for the 15-km mesoscale domain. The ensemble uses different combinations of physics schemes among its members (Table 2) to address the uncertainties in the model physics parameterization schemes (e.g., Stensrud et al. 2000, 2009b; Fujita et al. 2007; Wheatley et al. 2012). The diversity in physics options includes three cumulus parameterization schemes [Kain–Fritsch (Kain and Fritsch 1993; Kain 2004), Grell-3 (Grell and Devenyi 2002), and Tiedtke (Tiedtke 1989; Zhang et al. 2011b)], three planetary boundary layer (PBL) schemes [Yonsei University (YSU; Hong et al. 2006), Mellor–Yamada–Janjić (MYJ; Janjić 2002), and Mellor–Yamada–Nakanishi–Niino level 2.5 (MYNN2; Nakanishi and Niino 2006, 2009)], two shortwave (SW) radiation schemes [Dudhia (Dudhia 1989) and RRTMG (Iacono et al. 2008)], and two longwave (LW) radiation schemes [RRTM (Mlawer et al. 1997) and RRTMG (Iacono et al. 2008)]. The Thompson (Thompson et al. 2004, 2008) microphysics

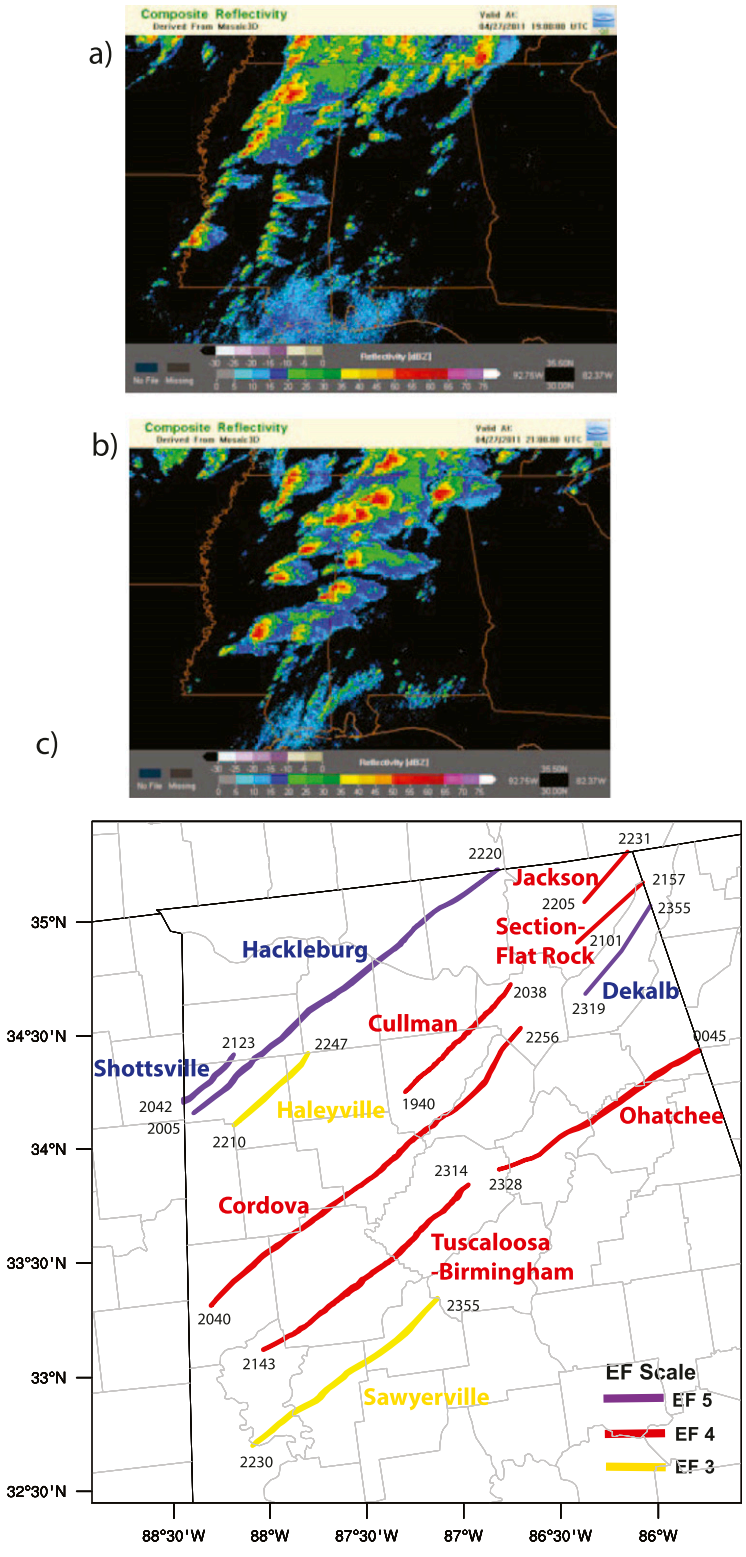

FIG. 1. (a) Composite reflectivity (dBZ, from the NSSL NMQ system) at 1900 UTC 27 Apr 2011 over the region of interest. (b) As in (a), but at 2100 UTC. (c) NWS damage swaths from north-central AL tornadoes (intensity ratings are indicated by colored lines; the start and end times for each swaths in UTC are labeled in black) during the afternoon and evening hours.

TABLE 1. The 11 significant tornadoes (EF3–EF5) over north-central AL between 1900 UTC 27 Apr and 0100 UTC 28 Apr 2011 [based on information from National Weather Service Birmingham (2014) and NOAA (2012)].

Tornado	Start time (UTC)	End time (UTC)	Duration (min)	EF	Length (km)
Cullman	1940	2038	58	4	75.4
Hackleburg–Phil Campbell–Tanner	2005	2220	135	5	212.4
Cordova	2040	2256	136	4	205.7
Shottsville	2042	2123	41	5*	59.7
Section–Flat Rock	2101	2157	56	4	75.6
Tuscaloosa–Birmingham	2143	2314	91	4	139.8
Jackson	2205	2231	26	4	48.7
Haleyville	2210	2247	37	3	51.2
Sawyerville–Eoline	2230	2355	85	3	116
DeKalb	2319	2355	36	5	59
Ohatchee	2328	0045	77	4	156.6

* EF5 rating based on damage in Mississippi.

and Noah (Tewari et al. 2004) land surface schemes are both fixed across the ensemble members. The physics options for both the parent and nested grid ensembles are identical except for the cumulus parameterization scheme, which is turned off on the storm-scale domain.

b. *Observation preprocessing*

The routinely available observations that are assimilated by the multiscale ensemble system are obtained from NOAA's Meteorological Assimilation Data Ingest System (MADIS). The observations assimilated in both meso- and storm-scale ensembles are the altimeter setting, temperature, dewpoint, and horizontal wind components from aviation routine weather reports (METARs), mesonet and marine surface stations, rawinsondes, aircraft, and satellite-derived winds. These MADIS observations are quality controlled using the MADIS processing and automated quality control (QC) procedure (as described online at http://madis.noaa.gov/madis_qc.html), which includes spatial and temporal consistency checks. The radar observations assimilated are the Doppler velocity and reflectivity from four WSR-88Ds (Fig. 2b): KBMX in Birmingham, Alabama; KHTX in Hytop, Alabama; KDGX in Jackson, Mississippi; and KGWX at Columbus Air Force Base, Mississippi. The raw level-II radar observations are obtained from the National Climatic Data Center (NCDC) and contain 14 scan angles (VCP-12 mode), completing each full volume scan in approximately 4.5 min. The reflectivity observations are quality controlled using the Quality Control Neural Network (QCNN; Lakshmanan et al. 2003) method to remove nonmeteorological echoes, anomalous propagation, and ground clutter. The Doppler velocity is dealiased using the method from Eilts and Smith (1990). The edited reflectivity and velocity observations are then objectively analyzed using the Observation Processing and Wind Synthesis (OPAWS; see Majcen et al. 2008) software. Any values of reflectivity below 0 dBZ are set to 0 dBZ and are assumed to represent "no precipitation," and radial velocity observations are omitted where the reflectivity is less than 20 dBZ. The radar observations are analyzed to 6-km grid spacing in the horizontal but on the original conical scan surfaces (Sun and Crook 2001; Dowell et al. 2004; Dowell and Wicker 2009), using a Cressman (1959) scheme. The "no precipitation" reflectivity observations are thinned to every 12 km (by skipping a grid point in each horizontal direction) to reduce the computational cost. Finally, the objectively analyzed radar observations are divided into 5-min bins and are assimilated at 5-min intervals.

c. *DART ensemble data assimilation and forecast system*

The data assimilation system used for this study is the ensemble adjustment Kalman filter (EAKF; Anderson 2001) from the Kodiak release branch (revision 5038) of the Data Assimilation Research Testbed software system (DART; Anderson and Collins 2007; Anderson et al. 2009).

1) MESOSCALE 1-H UPDATE SYSTEM

To create the mesoscale background, METAR, mesonet, marine, rawinsondes, aircraft, and satellite-derived winds from MADIS are assimilated into the ensemble every 1 h from 0100 UTC 27 April to 0000 UTC 28 April 2011 (Fig. 2c). Radar observations are not assimilated to create the mesoscale background. Both grids are run simultaneously in a one-way nested setup. The parent mesoscale ensemble provides the boundary conditions for the nested storm-scale ensemble. A half-radius of 230 km in the horizontal and a half-radius of 4 km in the vertical are used for the covariance localization function for the mesoscale ensemble [the fifth-order correlation

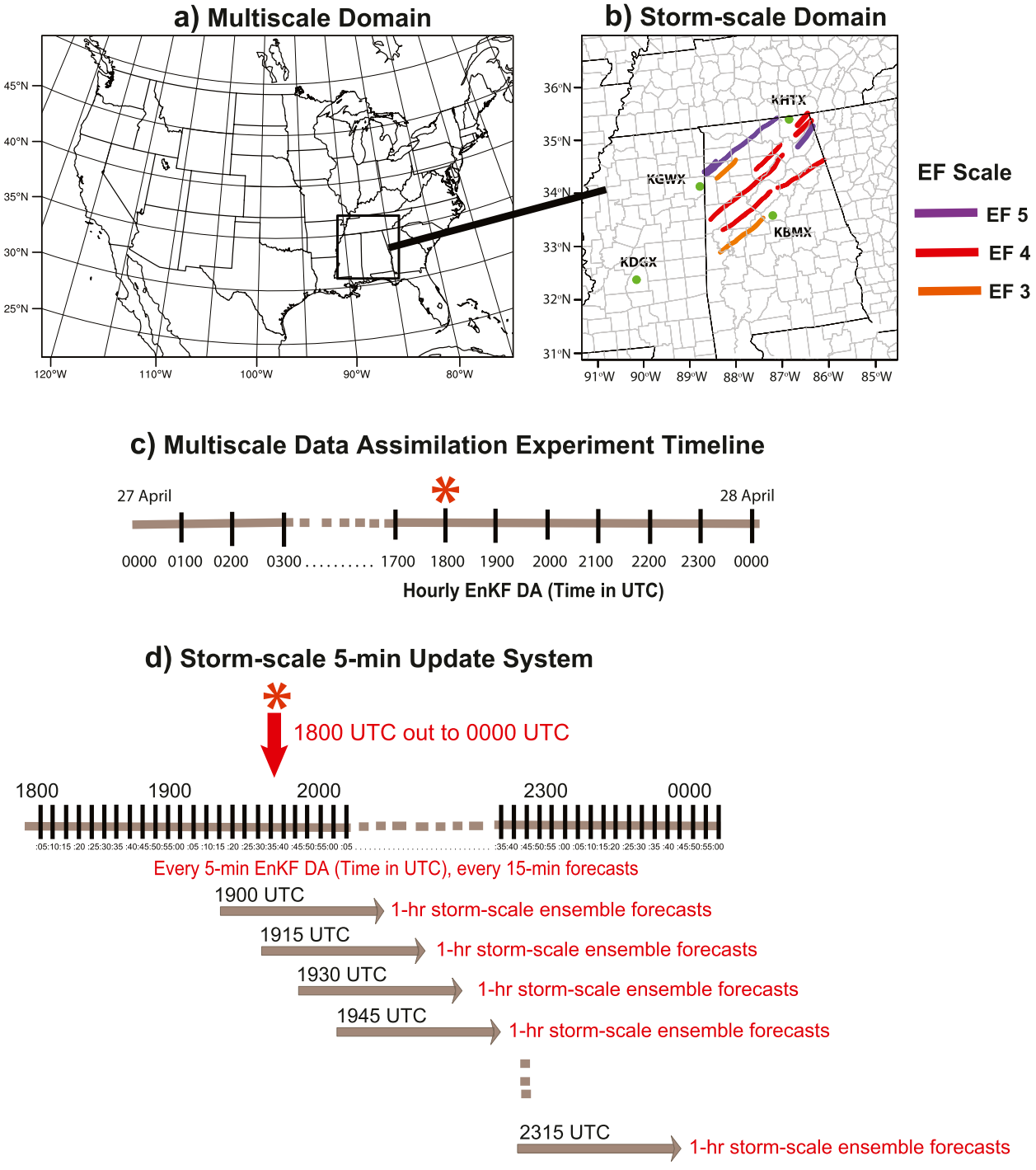

FIG. 2. (a) The multiscale domain with the 15-km horizontal grid-spacing mesoscale domain covering the CONUS and the nested 3-km storm-scale domain centered over northern AL. (b) The storm-scale domain enlarged with WSR-88D locations and color-coded tornado tracks, (c) the timeline of the hourly multiscale data assimilation experiments, and (d) the timeline for the storm-scale data assimilation and forecast experiments.

function from Gaspari and Cohn (1999)]. In addition, a temporally and spatially varying adaptive inflation (Anderson 2009) is applied at each assimilation cycle to the prior state space before the observations are assimilated to counteract the tendency of ensemble underdispersion. The filter implements additional observation quality control steps during assimilation such that if the magnitude of the difference between an

TABLE 2. Physics options for the multiphysics, multiscale WRF ensemble system. Here IC, BC, PBL, SW, and LW stand for initial conditions, boundary conditions, planetary boundary layer, and shortwave and longwave, respectively.

Multiphysics ensemble							
Ensemble member	GEFS member for ICs and BCs	Cumulus (15-km grid only)	Microphysics	PBL	Land surface	SW radiation	LW radiation
1	1	Kain–Fritsch	Thompson	YSU	Noah	Dudhia	RRTM
2	2			YSU		RRTMG	RRTMG
3	3			MYJ		Dudhia	RRTM
4	4			MYJ		RRTMG	RRTMG
5	5			MYNN2		Dudhia	RRTM
6	6			MYNN2		RRTMG	RRTMG
7	7	Grell-3	Thompson	YSU	Noah	Dudhia	RRTM
8	8			YSU		RRTMG	RRTMG
9	9			MYJ		Dudhia	RRTM
10	10			MYJ		RRTMG	RRTMG
11	11			MYNN2		Dudhia	RRTM
12	12			MYNN2		RRTMG	RRTMG
13	13	Tiedke	Thompson	YSU	Noah	Dudhia	RRTM
14	14			YSU		RRTMG	RRTMG
15	15			MYJ		Dudhia	RRTM
16	16			MYJ		RRTMG	RRTMG
17	17			MYNN2		Dudhia	RRTM
18	18			MYNN2		RRTMG	RRTMG
19	18	Kain–Fritsch	Thompson	YSU	Noah	Dudhia	RRTM
20	17			YSU		RRTMG	RRTMG
21	16			MYJ		Dudhia	RRTM
22	15			MYJ		RRTMG	RRTMG
23	14			MYNN2		Dudhia	RRTM
24	13			MYNN2		RRTMG	RRTMG
25	12	Grell	Thompson	YSU	Noah	Dudhia	RRTM
26	11			YSU		RRTMG	RRTMG
27	10			MYJ		Dudhia	RRTM
28	9			MYJ		RRTMG	RRTMG
29	8			MYNN2		Dudhia	RRTM
30	7			MYNN2		RRTMG	RRTMG
31	6	Tiedke	Thompson	YSU	Noah	Dudhia	RRTM
32	5			YSU		RRTMG	RRTMG
33	4			MYJ		Dudhia	RRTM
34	3			MYJ		RRTMG	RRTMG
35	2			MYNN2		Dudhia	RRTM
36	1			MYNN2		RRTMG	RRTMG

observation and prior ensemble mean exceeds 3 times the square root of the sum of the prior ensemble variance and observation error variance (i.e., an outlier threshold of 3.0), that observation is rejected (Liu et al. 2012). The assumed observation errors are the same as in Table 3 of Romine et al. (2013) except for METAR and marine temperature (1.75 K), METAR altimeter (0.75 hPa), and marine altimeter (1.20 hPa). The state variables updated by the data assimilation scheme include the three wind components, perturbation potential temperature, perturbation geopotential, perturbation surface pressure of dry air, and potential temperature tendency due to microphysics, as well as water vapor and all available hydrometeor fields (mixing ratios of cloud, rain, snow, ice, and graupel, and the number concentration of rain and ice) from the semi-double-moment Thompson microphysics scheme. In addition, the model-diagnosed 10-m horizontal wind components, 2-m temperature and water vapor, total surface pressure, and reflectivity are included in the model state for the filter, for the purpose of computing model priors in observation space.

2) STORM-SCALE CONTINUOUS 5-MIN UPDATE SYSTEM

As mentioned earlier, the focus of this study is on the northern Alabama severe weather outbreak that began around 1930 UTC and extended through the evening hours. To capture those supercells in the storm-scale analyses, the 1800 UTC 27 April storm-scale model

output from the hourly updated system is used as the background (prior) to assimilate radar, mesonet, METAR, radiosonde, and aircraft observations only on the storm-scale domain every 5 min for a 6-h period out to 0000 UTC the next day. The 15-km hourly updated mesoscale domain is used as the boundary conditions for the 3-km storm-scale 5-min update system.

All observations including radar and other conventional observations within each 5-min window are assumed to be valid at the central time. The no-precipitation reflectivity observations are assimilated to help suppress spurious convection that may develop in the model (Tong and Xue 2005; Aksoy et al. 2009; Dowell et al. 2011). Observation-error standard deviations are assumed to be 5 dBZ and 2 m s^{-1} for reflectivity and Doppler velocity, respectively. The covariance localization for the storm-scale ensemble is set to have a half-radius in the horizontal (vertical) of 9 (3) km for radar observations, 60 (3) km for mesonets, and 180 (3) km for other conventional observations. Additional spread to the storm-scale ensembles is provided by using the additive noise technique (Dowell and Wicker 2009). The additive noise technique is employed to add random, smooth, local perturbations every 15 min of the assimilation cycle to each ensemble member's horizontal wind components, temperature, and water vapor at locations where the observed radar reflectivity exceeds 40 dBZ. The additive noise is applied to the model state variables immediately before the updated ensemble is integrated forward in time. The perturbations have standard deviations of 0.50 m s^{-1} for horizontal winds and 0.50 K for temperature and dewpoint before smoothing (Dowell et al. 2011; Yussouf et al. 2013a). The spatial length scale for the perturbation smoothing function is 9 km in the horizontal and 6 km in the vertical.

To demonstrate what a WoF-type frequently updated forecast system might produce, 1-h ensemble forecasts with WRF history files every 5 min are initialized every 15 min starting from 1900 UTC, after 60 min of storm-scale data assimilation, and ending at 2315 UTC (Fig. 2d). The objective is to examine the quality of the analyses and very short-range ensemble probabilistic forecasts initialized from those analyses.

4. Results and discussion

a. Observation-space diagnostics

To quantitatively evaluate the overall performance of the assimilation system during the 6-h-long assimilation period from the 3-km storm-scale domain, observation-space diagnostic statistics (Dowell et al. 2004; Dowell and Wicker 2009; Yussouf et al. 2013a) of mean innovation (observation − model), root-mean square innovation (rmsi), total ensemble spread (standard deviation), and consistency ratio (from prior/background) are calculated using Eqs. (1)–(4) in Yussouf et al. (2013a). These statistics are calculated for the assimilated reflectivity and radial velocity observations (Fig. 3) from data in 5-min bins for the four WSR-88Ds. The mean innovation is a measure of the bias of the forecast–analysis with respect to the observations, the rmsi gives a measure of the overall fit of the forecasts and analyses to the observations, and the total spread gives information helpful for evaluating the sufficiency of ensemble spread for effective data assimilation. The reflectivity statistics are calculated for regions where the observed reflectivity is greater than 10 dBZ to isolate the performance measure around convective storms (Aksoy et al. 2009; Dowell et al. 2011; Dawson et al. 2012; Jung et al. 2012). As mentioned earlier, the radial velocity observations assimilated are already quality controlled to include radial velocity only where the observed reflectivity observations are greater than 20 dBZ. Therefore, no additional threshold is used to calculate the radial velocity statistics.

The mean innovation for reflectivity is comparatively larger (3–6 dBZ) during the initial spinup of the storm-scale ensemble (first ~30 min) and then starts to decrease with time and remains within the range of 1.5–2.5 dBZ (Fig. 3a). Clearly the model underpredicts the reflectivity during the entire assimilation period. Further investigation reveals that (not shown) after the initial model spinup, the mean reflectivity innovation is comparatively small (0–2 dBZ) at midlevels but varies between 2 and 4 dBZ near the surface and aloft, indicating underprediction of reflectivity. For radial velocity, the mean innovation (Fig. 3b) is very close to 0 (magnitude 0.6 m s^{-1} or less). The rmsi for reflectivity (Fig. 3a) starts with a higher value of 7–10 dBZ but decreases with subsequent assimilation cycles. After about 1 h of data assimilation, the rmsi for reflectivity becomes fairly stable. For radial velocity observations (Fig. 3b), the rmsi slightly increases during the later part of the assimilation period (possibly associated with increasing number, size, and/or amplitude of storms) but overall remains stable for the entire 6-h assimilation period.

The ensemble spread is representative of the forecast error only if the total spread and rmsi are of comparable magnitude, as indicated by the consistency ratio. A consistency ratio of ~1.0 indicates that the prior ensemble variance is a good approximation of the forecast error variance for the assumed observation error. The consistency ratio for reflectivity is smaller in early assimilation cycles, with initial values of 0.5 indicating insufficient spread, but increases with time to values

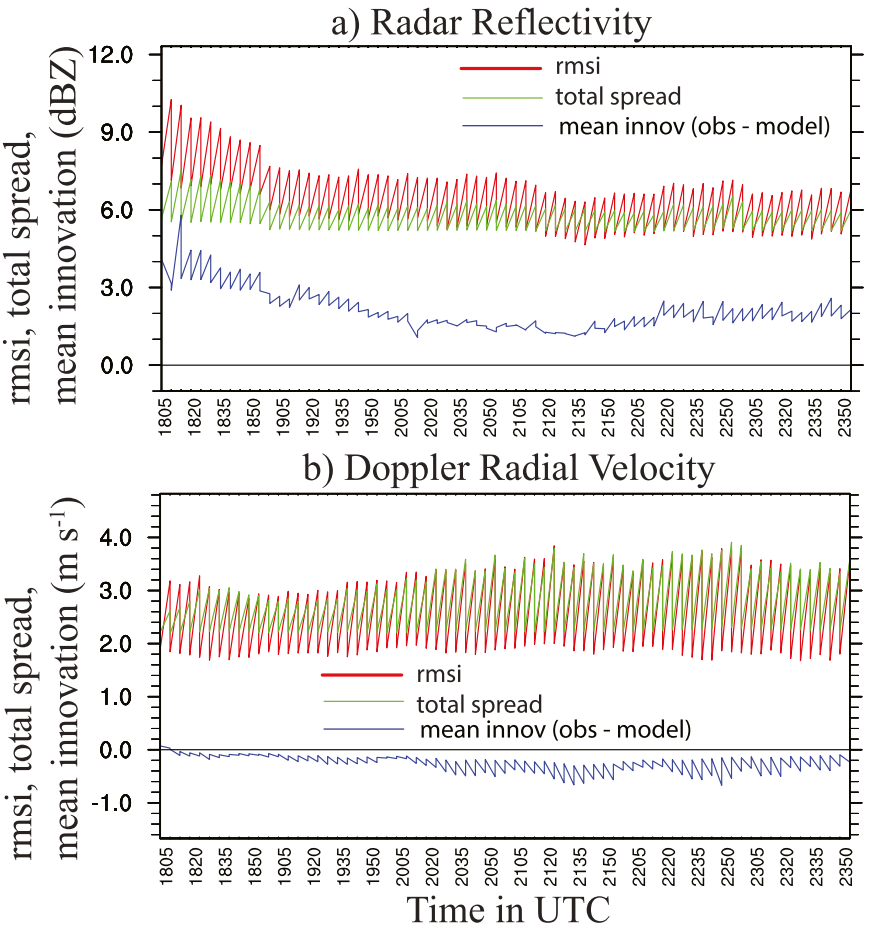

FIG. 3. Observation-space diagnostic statistics for assimilated (a) reflectivity (dBZ) and (b) Doppler velocity ($m\,s^{-1}$) observations from the four radars during the 6-h–every-5-min storm-scale data-assimilation period. Blue lines indicate mean innovation, red lines indicate the rmsi, and the green indicates the total ensemble standard deviation. The reflectivity statistics are computed only where the assimilated observed reflectivity is >10 dBZ. The sawtooth patterns are due to the plotted forecast and analysis statistics.

close to 0.8 (Fig. 4a). In general, ensemble underdispersion of reflectivity (Figs. 3a and 4a) is a common problem in real data assimilation studies at the convective scale (Aksoy et al. 2009; Snook et al. 2011, 2012; Jung et al. 2012; Yussouf et al. 2013a; Wheatley et al. 2014). In our study, the reflectivity bias of 1.5–6.0 dBZ (Fig. 3a) also leads to the consistency ratio being less than 1 because rmsi, the denominator of this ratio, includes contributions from bias errors.

The radial velocity observations maintain more favorable consistency ratios with initial values around 0.6 that increase rather quickly with subsequent assimilation cycles to values within a range of 0.9–1.1 (Fig. 4c). Importantly, the filter shows no sign of divergence during the 6-h-long continuous period of 5-min assimilation indicating robustness of the data assimilation system. The drop in the number of radar observations (Figs. 4b,d) at around 2220 UTC is due to the loss of communication and thus data loss from the KHTX radar at about 2216 UTC. The overall observation-space diagnostics (Figs. 3 and 4) suggest that the configuration parameters of the ensemble data assimilation system are fairly reasonable and stable.

b. *Reflectivity analyses and probabilistic forecasts*

To evaluate the overall structure, location, and intensity of the supercell storms from the continuous 6-h-long 5-min update system, the reflectivity analyses and forecasts from two representative times, specifically 1930 UTC (after 90 min of data assimilation) and 2130 UTC (after 210 min of data assimilation), are examined and compared with the observed reflectivity (Figs. 5 and 6). The reflectivity observations (shown in the first row in Figs. 5 and 6) are obtained from the National Mosaic

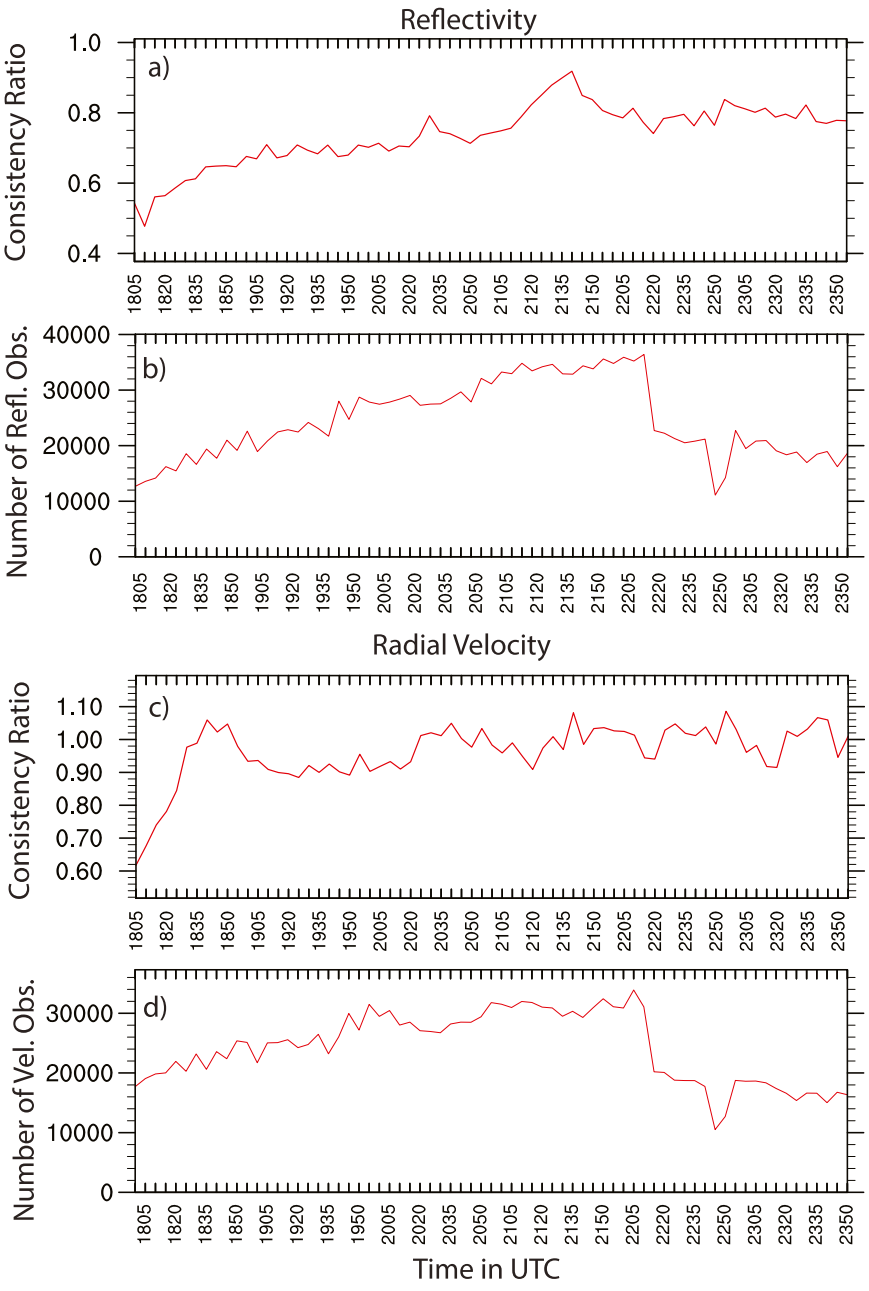

FIG. 4. The consistency ratio (calculated from the priors) and number of observations assimilated during the 6-h storm-scale data-assimilation period for (a),(b) reflectivity and (c),(d) Doppler velocity. The reflectivity statistics are computed only where the observed reflectivity is >10 dB*Z*.

and Multi-Sensor QPE (NMQ) 3D radar reflectivity mosaic (Zhang et al. 2011a) system. The NMQ reflectivity observations are initially gridded using 1-km grid spacing and so are thinned to 3-km grid spacing to match the storm-scale WRF grid. The reflectivity analyses (Figs. 5b and 6b) at 1.5 km above mean sea level (MSL) from an ensemble member reveal that the assimilation system is able to place the main supercells in the model at approximately the correct locations, as well as produce realistic supercell structures (e.g., curved shape and strong gradients) (Figs. 5a and 6a).

A positive aspect of the results from 1930 and 2130 UTC is the ability of the system to maintain strong supercell storms from the analyses well into the short-term forecasts (Figs. 5 and 6). The rapidly developing storm that impacted Cullman, Alabama, had just become

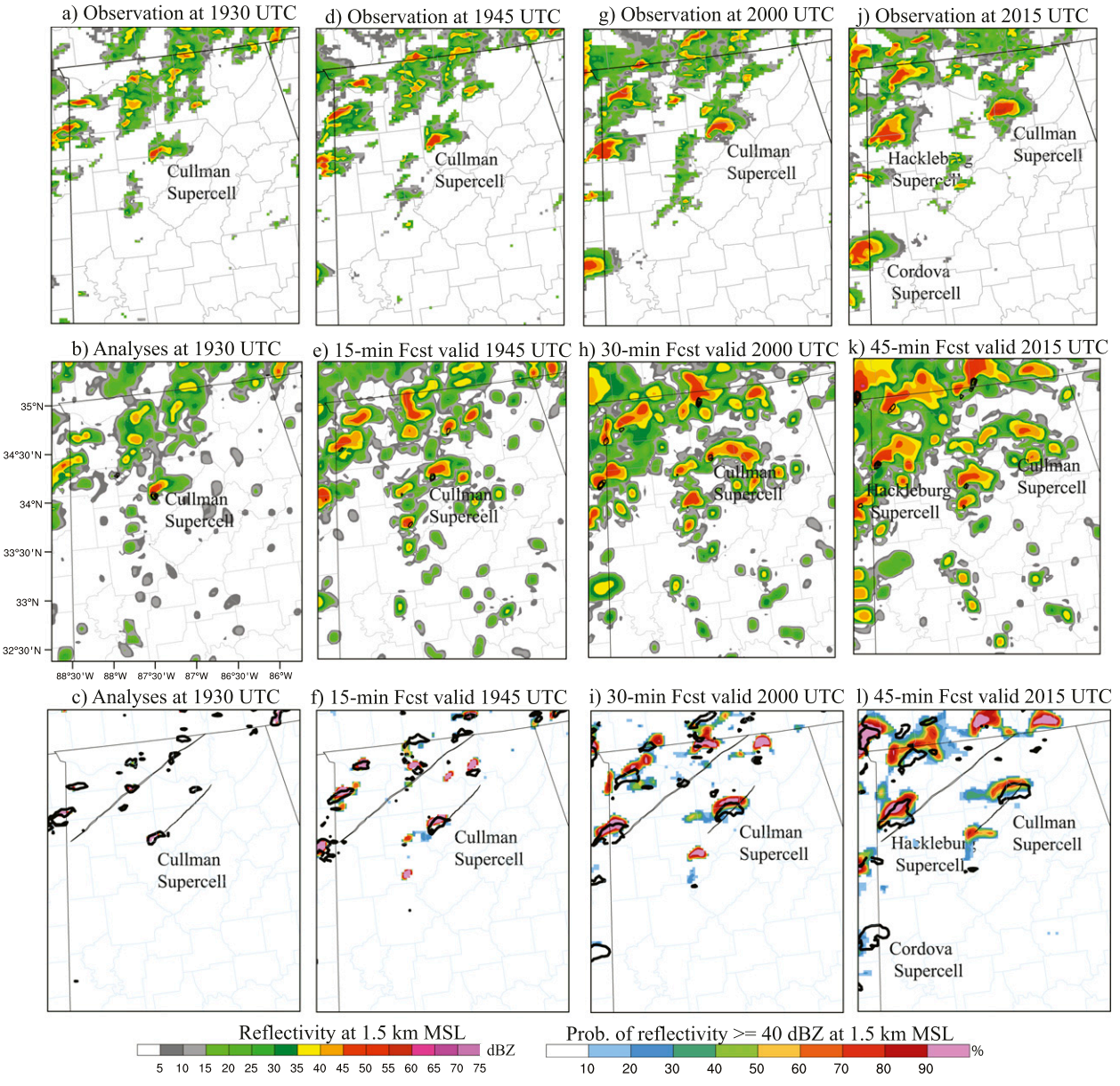

FIG. 5. (a),(d),(g),(j) The reflectivity observations (colors, 5-dBZ increment); (b),(e),(h),(k) analysis and every-15-min forecast from ensemble member 18 (black contours are the vertical vorticity from 0.003 to 0.008 s^{-1} at 0.001 s^{-1} interval at 1.5 km MSL); and (c),(f),(i),(l) the ensemble probability (colors, 10% increment) of reflectivity > 40 dBZ (thick black contours represent the observed 40-dBZ reflectivity) at 1.5 km MSL for the 45-min period beginning at 1930 UTC 27 Apr 2011. The thin black lines overlaid on each panel in (c),(f),(i), and (l) are the NWS-surveyed tornado damage paths. The portion of the domain shown here is over north-central AL.

a supercell before the 1930 UTC initialization time, and the ensemble forecast (Fig. 5) shows a strong signal for maintenance of this soon-to-be significant storm. In a typical member forecast, a low-level mesocyclone persists 30 min into the forecast (Figs. 5e,h). A probabilistic representation of the ensemble reflectivity forecasts shows high probabilities near the observed Cullman storm track throughout the forecast (Figs. 5f,i,l). The incipient Hackleburg storm had just developed a small, high-reflectivity core at 1930 UTC (not shown), but the forecasts clearly show its development into a significant storm as it enters into the northwest portion of the plotted domain (Figs. 5h,k,i,l).

Multiple significant supercells, including the Hackleburg, Cordova, and Tuscaloosa–Birmingham storms, were on going in northern Alabama at the 2130 UTC initialization time (Fig. 6). For these three storms, the 0–30-min forecast correctly shows maintenance of strong storms

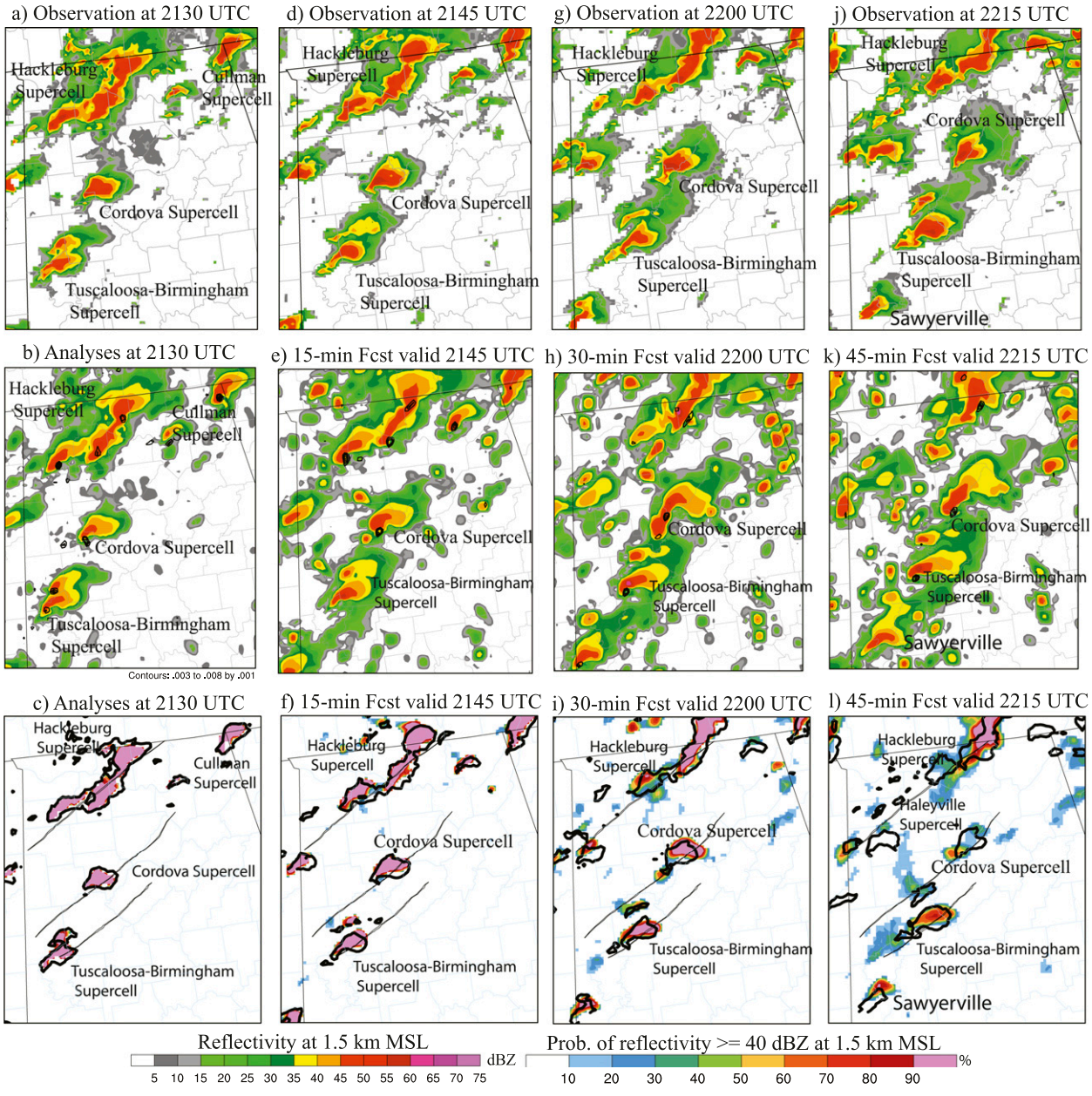

FIG. 6. As in Fig. 5, but for analyses at 2130 UTC.

with large, high-reflectivity cores and low-level rotation (Figs. 6e,h,k,f,i,l). On the other hand, a storm that produced an EF3 tornado in northwest Alabama (labeled "Haleyville" in Fig. 6l) is poorly forecast by the ensemble.

A problem seen previously in ensemble experiments with idealized model configurations (Tong and Xue 2005; Aksoy et al. 2009; Dowell et al. 2011, Lange and Craig 2014) and seen in the current case with full mesoscale complexity is the development of spurious convective cells in the forecast. Around the generally well-forecast main supercells, the individual ensemble members produce a number of small cells (Figs. 5e,h,k and 6e,h,k). Factors that may have contributed to the generation of spurious cells include incorporation of noise due to frequent observation assimilation, dynamical imbalance, or less consistent model dynamics at such high resolution (Lange and Craig 2014). In future work with this case, we will examine forecast sensitivity to the model configuration and data-assimilation procedures in an attempt to identify the most significant factors leading to spurious cells.

The last rows in Figs. 5 and 6 show the probability of reflectivity greater than 40 dBZ from the 36-member

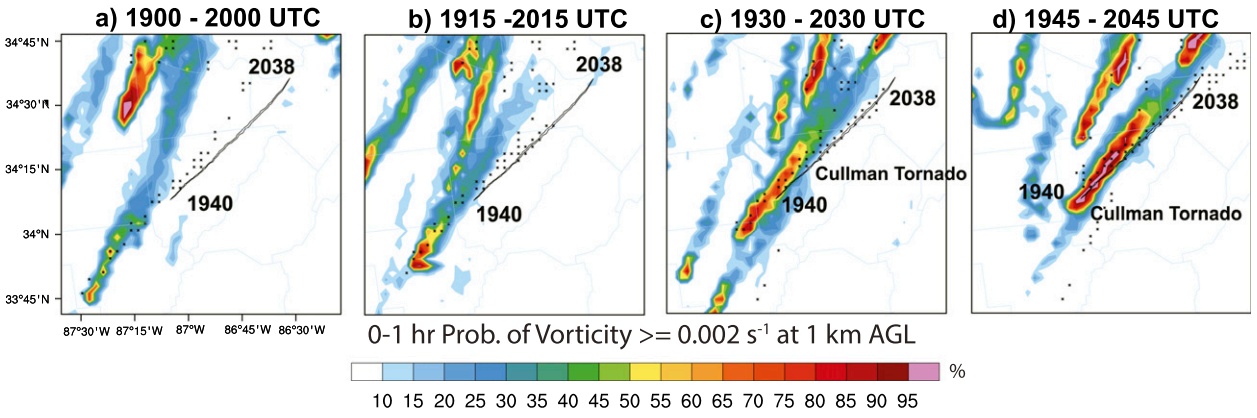

FIG. 7. The 1-h ensemble probability of vorticity exceeding a threshold of 0.002 s^{-1} at 1 km AGL for the Cullman supercell storm from the every-15-min analyses. Overlaid in each panel is the NWS-observed tornado damage track (gray outline, 1940–2038 UTC) and the WDSS-II-generated radar low-level (0–2 km AGL) mesocyclone rotation exceeding a threshold of 0.004 s^{-1} (black symbols) during the 0–1-h forecast periods.

ensemble at the analysis time (Figs. 5c and 6c) and then from forecasts every 15 min (Figs. 5f,i,l and 6f,i,l). The thick black contour is the observed 40-dBZ reflectivity contour, and the thin black lines overlaid on each panel are the NWS-surveyed tornado damage paths. Overall, the ensemble is successful at associating high probabilities with the dominant observed storms, but a closer inspection reveals some errors. The high probabilities of the model-generated storm cores are somewhat smaller than the observed storm cores (Figs. 5c and 6c,f), and some cores are even associated with zero probability in the forecast (Figs. 5f,i,l and 6i,l). Factors likely to play a role include model errors associated with physics parameterization schemes and model grid spacing. Furthermore, there are systematic displacement errors. Specifically, the forecast storms tend to move faster northeast than the observed storms. One possible factor for the displacement errors is the generation of too strong of a cold pool from reflectivity assimilation (Dowell et al. 2011; Yussouf et al. 2013a). Future work will investigate the reasons for the errors associated with the storm motion.

c. *Ensemble probabilistic forecasts of low-level rotation of the tornadic supercell storms*

The 3-km model horizontal grid spacing used in this study is far too coarse to explicitly resolve any tornado circulation, so instead we focus on mesocyclone forecasts. One good measure that can be used to infer the amount of low-level rotation within the rotating supercells from 3-km horizontal grid spacing models is the vertical vorticity (Stensrud and Gao 2010; Dawson et al. 2012; Stensrud et al. 2013; Yussouf et al. 2013a). To evaluate the capability of the 5-min update system to forecast low-level mesocyclones from supercell storms, the ensemble's probability of vertical vorticity at 1 km above ground level (AGL) is calculated (vorticity swaths). The 0–1-h forecast output (which is written out at 5-min intervals) from each ensemble member initialized from a certain analysis time is checked to see whether the vorticity exceeds a threshold value at the grid point at any output time, and the vorticity probabilities are calculated from the number of members exceeding the threshold values. A threshold of 0.002 s^{-1} is used for the vertical vorticity, which is a reasonable choice for grid-scale-based vorticity swaths at 3-km grid spacing (Yussouf et al. 2013a). Therefore, each of the swaths represents probabilistic forecasts of vorticity exceeding 0.002 s^{-1} at any time during the 1-h forecast period from the 36-member ensemble initialized at a certain analysis time. The idea is to see how well the ensemble system forecasts the low-level rotation swath of a particular storm with the observations assimilated so far. The probability forecasts of low-level rotation associated with some of the significant tornadic storms (tornadoes with EF ratings of 3 and higher) are examined and discussed below.

1) THE CULLMAN TORNADIC SUPERCELL

The first tornado that struck Alabama during the afternoon severe weather episode was the Cullman tornado. The tornado formed in western Cullman County at 1940 UTC [1440 central daylight time (CDT)] and tracked northeast through the heart of Cullman, a city of 15 000 people (TRAC 2012; NOAA 2012). The NWS rated the tornado EF4 with a pathlength of 75.4 km (Table 1). The 1-h forecast vorticity swaths for the Cullman storm are examined every 15 min for the 1900–1945 UTC initialization times, after 60–105 min of radar data assimilation (Figs. 7a–d). The swaths are compared against the NWS-surveyed damage track and the

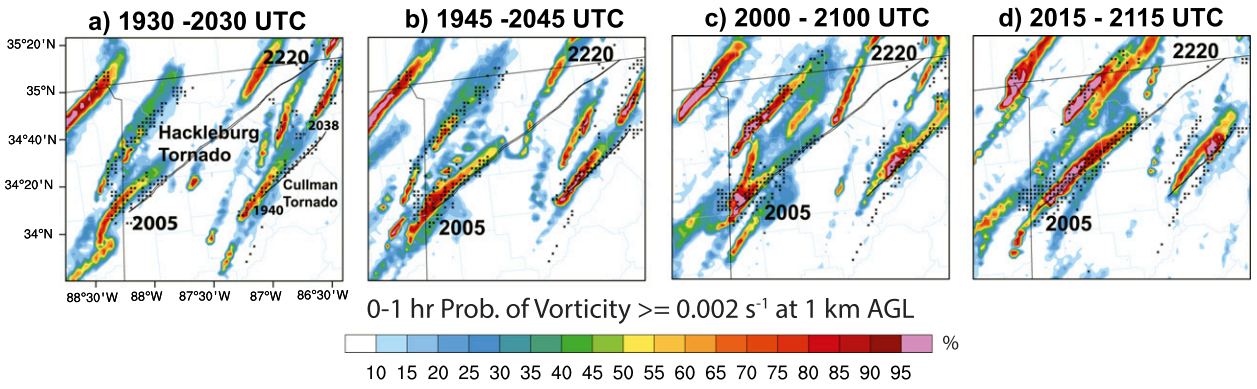

FIG. 8. As in Fig. 7, but for the Hackleburg tornado that starts at 2005 UTC and ends at 2220 UTC.

Warning Decision Support System–Integrated Information (WDSS-II; Lakshmanan et al. 2007) generated 0–2-km mesocyclone circulations (Miller et al. 2013) from the radar observations. The NWS damage track is shown by a gray line and the black symbols show the radar-derived circulation locations of vorticity 0.004 s^{-1} and higher during the 0–1-h forecast. The radar-derived rotation track and the NWS damage track complement and agree fairly well with each other, indicating that the combination of both can be used to compare how well the model performs in forecasting the low-level rotation of the supercells. However, caution must be exercised when comparing the model-generated low-level vorticity swaths with the observed NWS tracks and radar-derived WDSS-II circulations since these three quantities are not the same and may not always correlate well with tornado strength or even the existence of a tornado. The 1-h forecast probability of vorticity from the 1900 UTC ensemble (Fig. 7a), which is initialized 40 min before tornado formation, indicates zero low-level mesocyclone probability over the exact location where tornadogenesis occurred. However, the model forecasts high probabilities of low-level rotation (i.e., a rotating supercell) farther west and southwest, aligned with radar-observed rotation signatures of the pretornadic Cullman supercell (Fig. 7a). With an additional 15 min of data assimilation, the forecast vorticity swath (Fig. 7b) from 1915 UTC analyses, with probabilities as high as 40%, is still displaced to the west of the observed tornado damage track. The forecast probabilities for a strong low-level mesocyclone are increased with an additional 15 min of observation assimilation (Fig. 7c), and the forecast vorticity swath shifts eastward more toward the observed rotation and damage track compared to that initialized from the 1915 UTC analyses. The forecast vorticity probabilities from 1945 UTC analyses, the time when the tornado is occurring, reach values as high as 100% (Fig. 7d). The high probabilities along the mesocyclone track from the 1945 UTC forecast are more aligned with the observed Cullman mesocyclone and tornado damage tracks than the forecast probabilities from earlier lead times.

2) THE HACKLEBURG–PHIL CAMPBELL–TANNER TORNADIC SUPERCELL

Among the many tornadoes in northern Alabama, the Hackleburg tornado had the longest track. This tornado formed at 2005 UTC just inside the Mississippi–Alabama border in southwest Marion County. The tornado moved northeast through northern Alabama and into southern Tennessee, remaining on the ground for approximately 212 km before dissipating in Franklin County, Tennessee. This tornado was rated EF5 in Hackleburg and Phil Campbell, injuring at least 145 people and killing 72 more (TRAC 2012).

The forecast low-level vorticity swaths for the Hackleburg–Phil Campbell tornadic supercell are shown in Fig. 8. The left panel (Fig. 8a) is a 1-h forecast from the 1930 UTC analysis ensemble, initialized 35 min before the tornado formed. Several supercells traversed from eastern Mississippi to northern Alabama and portions of southern middle Tennessee during that time. The 1-h forecast from 1930 UTC shows a low-level mesocyclone track, with probabilities as high as 85%, which overlaps with the radar-derived rotation but to the left (northwest) of the observed Hackleburg damage path. During the forecast period, another smaller cell over eastern Mississippi matured into a rotating supercell, moved northeast, and produced low-level rotation during the last 15-min forecast period with probabilities as high as 80% (the shorter swath at the lower left in Fig. 8a). The forecast initialized at 1945 UTC (Fig. 8b), after three more assimilation cycles, shows the dominant high-probability swath with values as high as 95%; the storm path remains somewhat to the left of the observed Hackleburg damage track. Attached to the

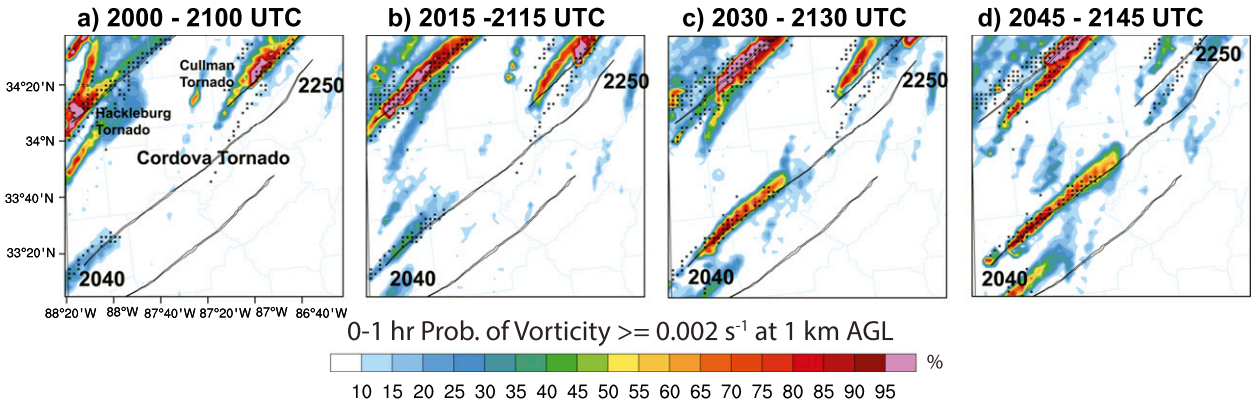

FIG. 9. As in Fig. 7, but for the Cordova tornado that starts at 2040 and ends at 2250 UTC.

southwestern end of the high-probability swath is a parallel lower-probability swath straddling the Mississippi–Alabama border. In reality, radar data indicate two developing storms in close proximity between 1940 and 2000 UTC (not shown). From an additional 15 min of observation assimilation between 1945 and 2000 UTC, the ensemble changed its depiction about which of the pair of storms would dominate, now associating the high probability swath (Fig. 8c) with the observed storm that would soon produce the Hackleburg tornado. The vorticity probabilities are highest early in the forecast, approaching 100%, and gradually decreasing with time. The ensemble forecast from 2015 UTC (Fig. 8d) increases the extent of high probabilities of low-level rotation and also aligns the swath more along the observed rotation and damage track. Overall, the forecast probabilities of a strong low-level mesocyclone are consistently increased with each additional assimilation cycle for the Hackleburg tornadic storm.

To the northwest of the Hackleburg track is another model-generated high-probability vorticity swath (Figs. 8c,d) that aligns well with the radar-derived rotation. There was indeed a rotating supercell along that swath, but no tornado was detected with that storm, in real time or after the fact. This storm is included in an ongoing investigation, to be reported upon in a future paper, about whether it might be possible to differentiate between tornadic and nontornadic supercells at grid resolutions that do not explicitly resolve tornado-scale circulations. A storm even farther northwest that produced a short-lived tornado, indicated by probability swaths in Fig. 8 from northeast Mississippi to southwest Tennessee, is outside the domain of our study.

3) THE CORDOVA TORNADIC SUPERCELL

The long-track, violent Cordova tornado formed at 2040 UTC and passed through Pickens, Tuscaloosa, Fayette, Walker, Cullman, Blount, and Marshall Counties of Alabama along its 205-km path over 2 h and 10 min (TRAC 2012). This tornado achieved a maximum intensity of EF4 and resulted in 54 injuries and 13 fatalities. The supercell that produced the Cordova tornado later produced another violent (EF5) tornado, which formed at 2319 UTC over DeKalb County (Table 1).

The 1-h ensemble probabilistic vorticity forecast from the 2000 UTC analyses (Fig. 9a), initialized 40 min before tornadogenesis, shows some sign of mesocyclones along the radar-derived Cordova rotation track but with low probabilities (10%–30%). After 15 min, the forecast probabilities are increased to as high as 50% (Fig. 9b). At 2030 UTC, which is 10 min before tornadogenesis, the ensemble forecast shows probability values as high as 90% (Fig. 9c), and these high probabilities are maintained and even increased to higher than 95% in some places later for the ongoing tornadic supercell (Fig. 9d).

4) THE TUSCALOOSA–BIRMINGHAM TORNADIC SUPERCELL

The Tuscaloosa–Birmingham tornado was the deadliest tornado of the day, causing 65 fatalities and injuring around 1500 people along its 140-km path from Tuscaloosa to the Birmingham suburbs. The tornado developed at 2143 UTC southwest of Tuscaloosa, then exited the Tuscaloosa metropolitan area and tracked east-northeast toward Birmingham. Just 14 min after the Tuscaloosa–Birmingham tornado finally lifted at 2314 UTC, the parent Tuscaloosa–Birmingham supercell spawned another violent tornado (the EF4 Ohatchee tornado at 2328 UTC; Table 1).

Instead of 1-h forecast vorticity swaths, the forecasts shown in Fig. 10 extend out to 2315 UTC, which is the end time of the tornado. The forecast lengths range from 135 min in the top row (forecasts initialized at 2100 UTC, which is 43 min before tornadogenesis) to 90 min in the

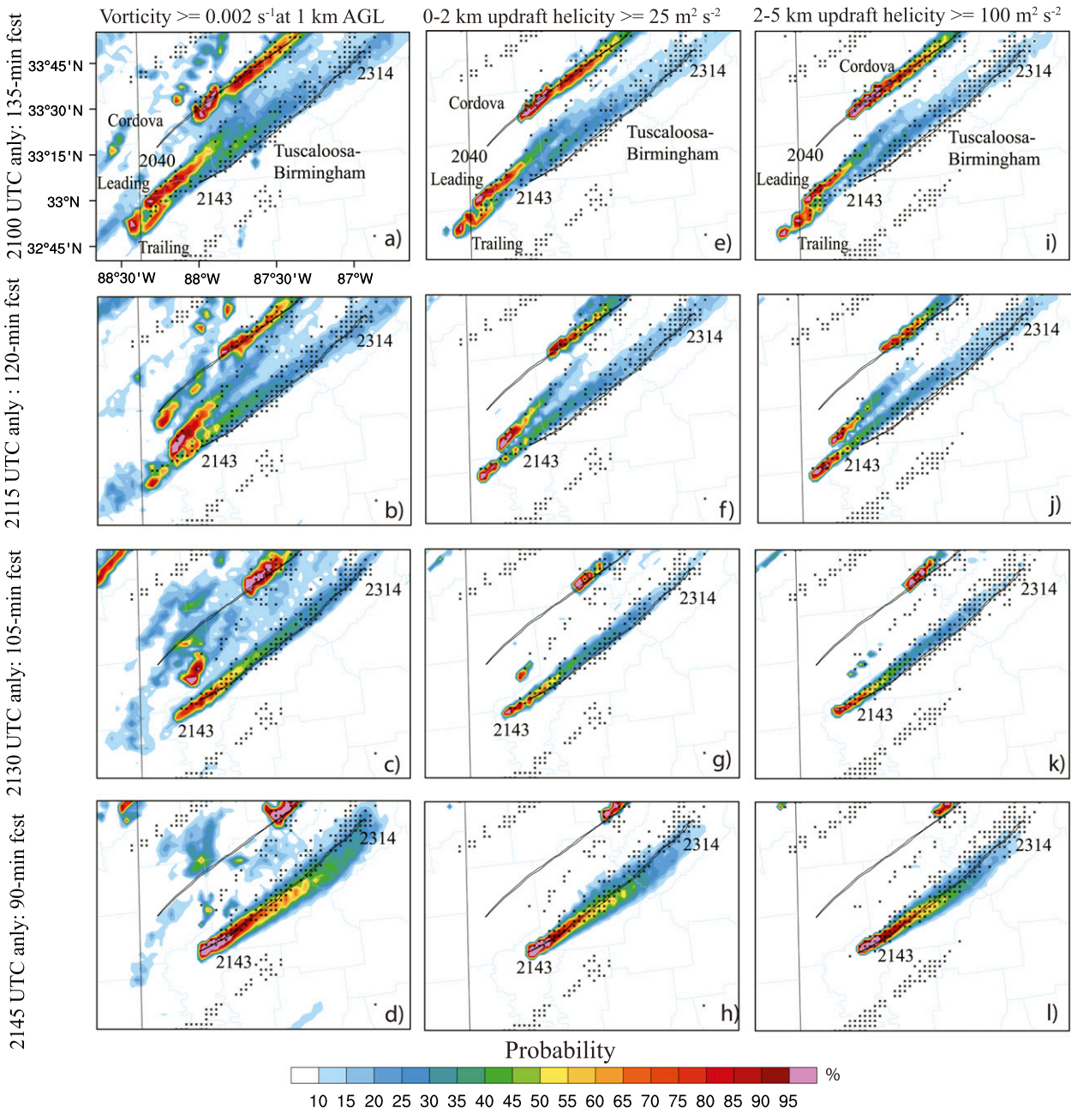

FIG. 10. (a)–(d) Ensemble probability of vorticity forecasts exceeding a threshold of 0.002 s^{-1} at 1 km AGL, (e)–(h) the 0–2-km updraft helicity exceeding a threshold of 25 $m^2 s^{-2}$, and (i)–(l) the 2–5-km updraft helicity exceeding a threshold of 100 $m^2 s^{-2}$ from (top to bottom) the every-15-min analyses for the Tuscaloosa–Birmingham supercell. Overlaid in each panel is the NWS-observed tornado damage track (gray outline) and the WDSS-II-generated radar-derived low-level (0–2 km AGL, left and middle columns) and midlevel (2–5 km AGL, right column) mesocyclone exceeding a threshold of 0.004 s^{-1} (black symbols) during the indicated forecast periods.

bottom row (forecasts initialized at 2145 UTC, the time of tornadogenesis). Thus, the forecast vorticity swaths cover the entire lifetime of the Tuscaloosa–Birmingham tornado. In addition to the probabilities of vorticity exceeding a 0.002 s^{-1} threshold (first column), grid-scale probabilities of updraft helicity exceeding a threshold (UH; Kain et al. 2008; Clark et al. 2012, 2013; Yussouf et al. 2013b) over 0–2 km (low level) and 2–5 km (midlevel) AGL also are calculated. The thresholds used in Fig. 10 for low- and midlevel UH are 25 (second column) and 100 $m^2 s^{-2}$ (third column), respectively, and these threshold values are reasonable choices for

identifying significant low-level mesocyclonic features at 3-km grid spacing (Carley et al. 2011; Trapp et al. 2011).

For the four initialization times shown, variability in the vorticity/helicity swaths near Tuscaloosa and Birmingham appears to be related to different forecast scenarios for a pair of storms in close proximity (not shown). We will call these the lead storm and the trailing storm. The trailing storm, which was the storm that eventually dominated and produced the Tuscaloosa–Birmingham tornado, was to the southwest of the lead storm at 2100 UTC. The forecasts from 2100 UTC show probabilities of strong low-level rotation with values as high as 100% (Figs. 10a,e,i) for the leading storm, but the vorticity swath is displaced to the west-northwest of the tornado damage track. At this time, the probabilities of low-level rotation for the trailing storm are lower on average along the swath than for the leading storm, but the swath overlaps with the radar-derived circulations and aligns along the entire Tuscaloosa–Birmingham observed track. The probability forecast initialized 15 min later (Figs. 10b,f,j) still shows well-defined swaths associated with both the leading and trailing storms. After three more assimilation cycles (i.e., 15 min later), the ensemble forecast initialized at 2130 UTC (Figs. 10c,g,k) clearly emphasizes the trailing storm, showing swaths of vorticity/helicity exceeding the thresholds with probabilities greater than 15% along the entire Tuscaloosa–Birmingham observed track. While there are still indications of low-level rotation with probabilities greater than 65% for the leading storm (Figs. 10c,g), the midlevel rotation has dissipated by this time (Fig. 10k). By the 2145 UTC initialization time, probabilities have become high along the entire radar-derived rotation track, and there have been refinements in the location of the axis of highest probabilities.

The vorticity swath plots shown in Figs. 7–10 are calculated using raw gridpoint probabilities. However, since high-resolution NWP models typically are not skillful at grid scale, a common practice (Schwartz et al. 2010; Snook et al. 2012; Yussouf et al. 2013a,b; Potvin and Wicker 2013; Schwartz et al. 2014; Schumacher and Clark 2014) is to use a neighborhood-based approach in calculating probabilities to account for small spatial and temporal errors. We compare the raw gridpoint-based probabilities (Fig. 10) to neighborhood probabilities (Fig. 11) for the Tuscaloosa–Birmingham tornado. We apply a neighborhood with a radius of influence of 9 km around the grid points (Snook et al. 2012; Yussouf et al. 2013a,b) and generate Fig. 11, which is similar to Fig. 10 but using thresholds of $0.004\,s^{-1}$ for vorticity (first column), $50\,m^2\,s^{-2}$ for 0–2 km AGL UH (second column), and $150\,m^2\,s^{-2}$ for 2–5 km AGL UH (third column) to calculate the probabilities. Overall, the results show that the neighborhood-based (Fig. 11) forecast probabilities are higher (with wider swaths) compared to those from the gridpoint-based probabilities (Fig. 10), indicating that the selection of specific neighborhood parameters (e.g., radius of influence, thresholds, etc.) can sometimes inflate the forecast probabilities. Moreover, the neighborhood-based probabilities can make the inspection of the two nearby swaths from two rotating storms less obvious (Figs. 11a–c, 11e–g, and 11i–k). Another interesting aspect of the neighborhood-based approach is the spatial uncertainty associated with the mesocyclone position. For example, the forecast probability at the end of the Tuscaloosa–Birmingham tornado swath from the 2145 UTC analyses has gridpoint probability values of ~10% (Fig. 10d), while the neighborhood-based approach shows probability values of ~50% (Fig. 11d). However, the spatial uncertainty is very different at the start of the swath where the storm position is known very accurately, yet the same neighborhood approach is applied to all points within the 1-h forecast, indicating that the "cone of uncertainty" should expand with time. Therefore, the neighborhood approach should account for the spatial uncertainties in the forecast with increasing lead time as the storm tracks diverge in time. This is a crucial part of developing probabilistic guidance for WoF-type systems and needs to be investigated further in the future.

The forecasts of low- and midlevel UH swaths for other tornadic supercells discussed above are very similar to the vorticity swaths and hence are not shown. Using UH track as a proxy for tornado pathlength forecasts, Clark et al. (2013) showed in other storm-scale model forecasts for this case that the UH forecast pathlength was strongly related to the track length of the observed tornadoes.

5) Frequent 1-h forecast vorticity swaths from the 5-min update system

Warn-on-Forecast systems will assimilate the most recently available observations of ongoing convection and provide ensemble forecasts frequently (Stensrud et al. 2009a). To evaluate if such systems are plausible, 1-h ensemble forecasts were produced every 15 min from the continuous 5-min storm-scale update system. The forecast probabilities of vorticity exceeding $0.002\,s^{-1}$ at 1 km AGL are generated from initializations as early as 1900 UTC, which is after 60 min of radar data assimilation, and the last forecast is initialized at 2315 UTC (Fig. 12). During this time period, 11 significant tornadoes with ratings ranging from EF3 to EF5 occurred over north-central Alabama (Table 1). The NWS damage tracks in Fig. 12 are overlaid on each panel if that particular tornado was occurring during that forecast period.

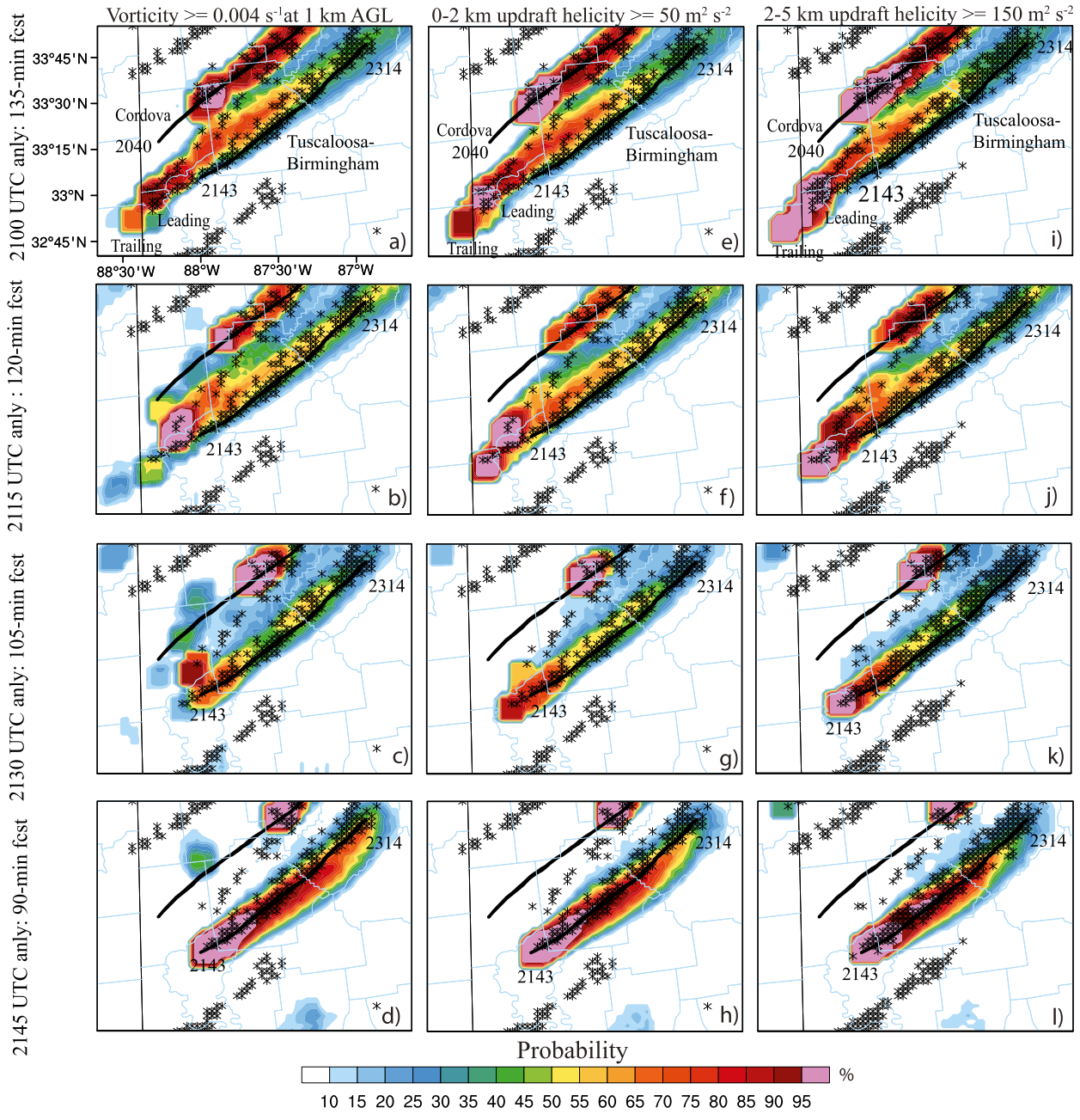

FIG. 11. As in Fig. 10, but using a neighborhood approach with a radius of 9 km to create the ensemble probability of (a)–(d) vorticity forecasts exceeding a threshold of 0.004 s^{-1} at 1 km AGL, (e)–(h) the 0–2-km updraft helicity exceeding a threshold of 50 $m^2 s^{-2}$, and (i)–(l) the 2–5-km updraft helicity exceeding a threshold of 150 $m^2 s^{-2}$ from (top to bottom) the every-15-min analyses for the Tuscaloosa–Birmingham supercell. The overlaid NWS-observed tornado damage track (gray outline) and the WDSS-II-generated mesocyclone rotation (black symbols) exceeding a threshold of 0.004 s^{-1} are the same as in Fig. 10 but here are plotted using larger thickness for better readability.

We quantify the forecast lead time (how early the ensemble system is able to indicate low-level rotation) over the genesis locations of the 11 significant tornadoes for forecast probabilities of vorticity greater than 10% and 50% (from the 1-h forecasts at the every-15-min intervals in Fig. 12) in Table 3. This simple method of quantifying forecast results focuses on the ensemble's ability to develop rotating storms from incipient convective cells and to maintain existing mature supercells. The case of interest here is generally considered to

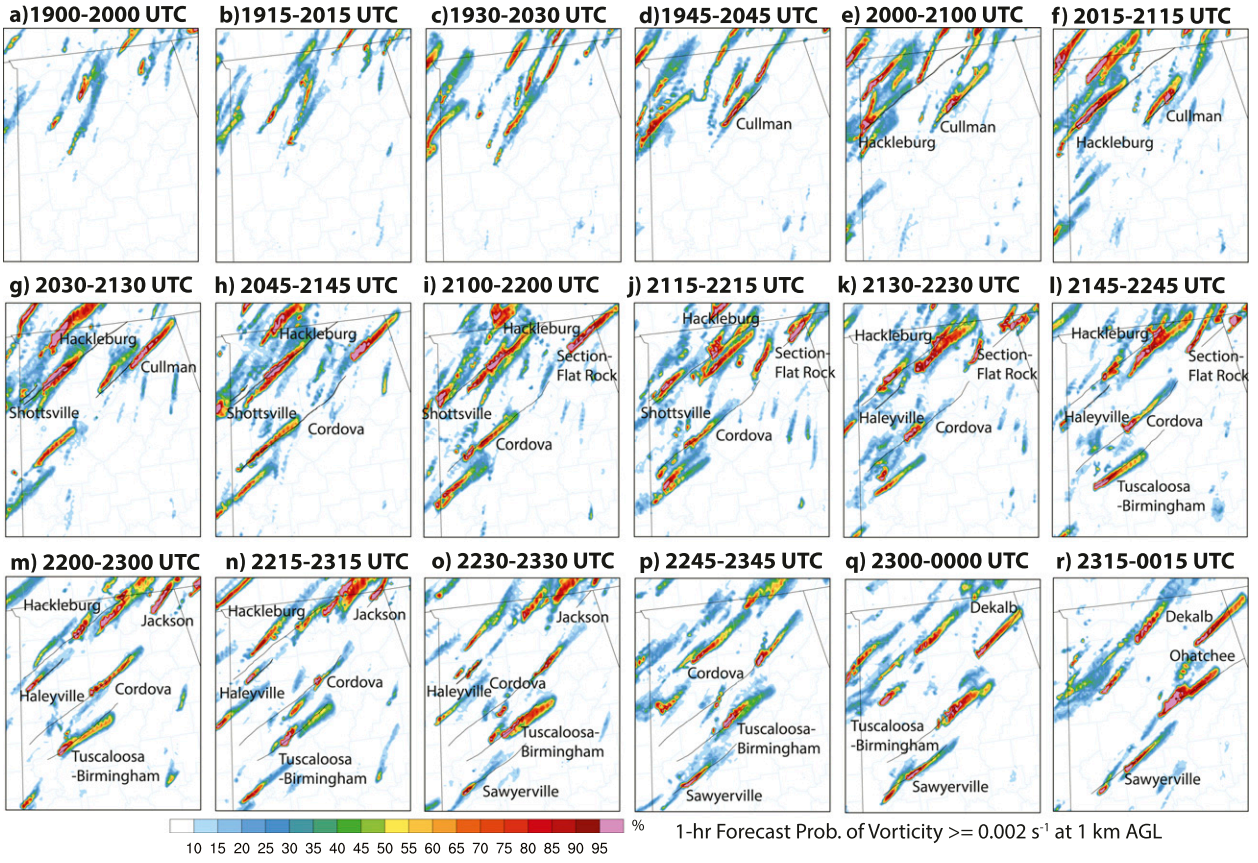

FIG. 12. The 1-h ensemble probability of vorticity forecasts exceeding a threshold of 0.002 s^{-1} at 1 km AGL starting from (top left) 1900 UTC analyses and then from the every-15-min analyses out to (bottom right) 2315 UTC. Overlaid in each panel is the NWS-observed tornado damage track (gray outline).

have a high degree of predictability (NOAA 2012). During the coming years, WoF prototypes will be tested for more cases and verified with more comprehensive statistics that also include false alarm rate and account for the reduction in lead time associated with forecast latency.

In general, the forecast probabilities show signs of low-level mesocyclone development downstream of incipient and mature storms, corresponding roughly to observed tornado tracks, for forecast lead times averaging 35 min (as high as 58 min) with probabilities greater than 10%, and for forecast lead times averaging 18 min (as high as 31 min) with probabilities greater than 50% (Table 3). The lead times vary considerably among the 11 tornadoes, an issue that must be investigated in future studies with more cases. With each additional assimilation cycle, the forecast probabilities of a strong low-level mesocyclone are generally increased, and the swath of highest probabilities is more aligned with the observed storm track. For the Section–Flat Rock, Tuscaloosa–Birmingham, and Ohatchee tornadic events, the system performs reasonably well in forecasting vorticity swaths with probabilities greater than 50% at longer lead times (28+ min). But for tornadic events like Cullman, Cordova, and Haleyville, the lead times for 50% probabilities are 10 min or less. Indeed, significant research efforts are needed to address the challenges of generating accurate forecasts of low-level rotation even at 30-min lead times. Overall, results for the several tornadoes examined here could suggest there is some hope for useful operational guidance in tornado warnings provided by continuously cycled NWP ensembles. This concept will be investigated in future work with other cases across a spectrum of storm environments and storm modes.

5. Summary and conclusions

One aspect of the WoF project is the numerical-model-based probabilistic storm-scale analysis and forecast of hazardous convective weather events to support the warning operations within NOAA (Stensrud et al. 2009a). To evaluate if such a system is plausible, a WRF-ARW model ensemble with a multiscale EAKF

TABLE 3. Forecast lead time (in minutes) for low-level mesocyclone probabilities >10% and 50% over the genesis locations of the 11 significant tornadoes (Table 1) during the study period (from the 1-h forecasts of vorticity $>0.002\,s^{-1}$ at 15-min intervals in Fig. 12).

Tornado	Lead time for >10% (min)	Lead time for >50% (min)
Cullman	25	10
Hackleburg–Phil Campbell–Tanner	20	20
Cordova	40	0
Shottsville	42	12
Section–Flat Rock	46	31
Tuscaloosa–Birmingham	58	28
Jackson	20	20
Haleyville	*10	10
Sawyerville–Eoline	15	15
DeKalb	49	19
Ohatchee	58	28

* Although probabilities >10% are predicted over the genesis location earlier than 2200 UTC, a well-defined swath is not predicted until the forecast from 2200 UTC.

data assimilation and forecast system was developed and tested for the 27 April 2011 Alabama outbreak of tornadic supercells. The goal was to see how well this continuous 5-min update system performed in predicting the probabilities of low-level rotation for widespread tornadic supercells during the 6-h assimilation period.

Observation-space diagnostic statistics reveal that the filter shows no sign of forecast divergence during the 6-h assimilation period, indicating the robustness of the data assimilation system. The consistency ratio for reflectivity is smaller in early assimilation cycles but increases with time while the radial velocity observations maintain more favorable consistency ratios with values near ~1.0. The assimilation system is able to analyze the main supercells in the model at approximately the correct locations with realistic supercellular structure and maintains the supercellular structure with low-level rotation during the 1-h forecast period. However, the model produces many spurious smaller cells during the 0–1-h forecast period that are not observed. The short-range probability forecasts of reflectivity greater than 40 dBZ show that the ensemble is successful at associating high probabilities with the dominant observed storms. However, the model-generated storm cores are somewhat smaller than the observed storm cores, indicating that there are errors in the model forecasts. The forecast storms also tend to move faster than the observed storm with a northeast displacement error. One major source of forecast error in storm-scale modeling is the model error. To understand and reduce model errors associated with spurious cells and biases in storm motion, we will conduct additional analyses and sensitivity experiments in the future.

The grid-scale and neighborhood ensemble forecast probabilities of strong low-level mesocyclones of the tornadic supercell storms during the 6-h period are encouraging. The system is able to predict consistently (i.e., with little variability from one forecast to the next) the low-level mesocyclones of the significant isolated tornadic supercells. For cases with multiple interacting storms in close proximity, the system tends to produce more variability in mesocyclone forecasts from one initialization time to the next until the observations show the dominance of one of the cells. Overall, there is a consistent and gradual increase with time in the probabilities of low-level mesocyclone forecasts from the continuous 5-min storm-scale update system with forecast lead times averaging 35 and 18 min for the 10% and 50% probability thresholds, respectively, for the 11 tornadic supercells examined. Within the context of the WoF paradigm, the overall encouraging results obtained from this study provide reasons for cautious optimism and motivate us to conduct future studies on how to reduce model errors (e.g., storm-motion errors and spurious storms) and to design storm-scale ensembles that better represent typical 1-h forecast errors.

Acknowledgments. Thanks to Chris Karstens for helping with the WSR-88D radar data quality control. The computing for this project was performed at the University of Oklahoma (OU) Supercomputing Center for Education and Research (OSCER). Thanks to Carrie Langston for the NMQ reflectivity data. The authors also would like to thank WRF Help at the National Center for Atmospheric Research (NCAR) for their user support and staff from the Data Assimilation Research Section (DAReS), particularly Glen Romine, who developed earlier prototype WRF-DART ensemble systems and provided comments on this work. The constructive comments of three anonymous reviewers greatly improved the manuscript. Local computer assistance is provided by Brett Morrow, Steven Fletcher, Brad Swagowitz, and Karen Cooper. Partial funding for this research was provided by NOAA/Office of Oceanic and Atmospheric Research under NOAA–University of Oklahoma Cooperative Agreement NA17RJ1227, U.S. Department of Commerce.

REFERENCES

Aksoy, A., D. Dowell, and C. Snyder, 2009: A multicase comparative assessment of the ensemble Kalman filter for assimilation of radar observations. Part I: Storm-scale analyses. *Mon. Wea. Rev.,* **137,** 1805–1824, doi:10.1175/2008MWR2691.1.

——, ——, and ——, 2010: A multicase comparative assessment of the ensemble Kalman filter for assimilation of radar observations. Part II: Short-range ensemble forecasts. *Mon. Wea. Rev.,* **138,** 1273–1292, doi:10.1175/2009MWR3086.1.

Anderson, J. L., 2001: An ensemble adjustment filter for data assimilation. *Mon. Wea. Rev.,* **129,** 2884–2903, doi:10.1175/1520-0493(2001)129<2884:AEAKFF>2.0.CO;2.

——, 2009: Spatially and temporally varying adaptive covariance inflation for ensemble filters. *Tellus,* **61A,** 72–83, doi:10.1111/j.1600-0870.2008.00361.x.

——, and N. Collins, 2007: Scalable implementations of ensemble filter algorithms for data assimilation. *J. Atmos. Oceanic Technol.,* **8,** 1452–1463, doi:10.1175/JTECH2049.1.

——, T. Hoar, K. Raeder, H. Liu, N. Collins, R. Torn, and A. Avellano, 2009: The Data Assimilation Research Testbed: A community facility. *Bull. Amer. Meteor. Soc.,* **90,** 1283–1296, doi:10.1175/2009BAMS2618.1.

Carley, J. R., B. R. J. Schwedler, M. E. Baldwin, R. J. Trapp, J. Kwiatkowski, J. Logsdon, and S. J. Weiss, 2011: A proposed model-based methodology for feature-specific prediction for high-impact weather. *Wea. Forecasting,* **26,** 243–249, doi:10.1175/WAF-D-10-05008.1.

Clark, A. J., J. S. Kain, P. T. Marsh, J. Correia, M. Xue, and F. Kong, 2012: Forecasting tornado pathlengths using a three-dimensional object identification algorithm applied to convection-allowing forecasts. *Wea. Forecasting,* **27,** 1090–1113, doi:10.1175/WAF-D-11-00147.1.

——, J. Gao, P. T. Marsh, T. Smith, J. S. Kain, J. Correia, M. Xue, and F. Kong, 2013: Tornado pathlength forecasts from 2010 to 2011 using ensemble updraft helicity. *Wea. Forecasting,* **28,** 387–407, doi:10.1175/WAF-D-12-00038.1.

Cressman, G. P., 1959: An operational objective analysis system. *Mon. Wea. Rev.,* **87,** 367–374, doi:10.1175/1520-0493(1959)087<0367:AOOAS>2.0.CO;2.

Dawson, D. T., II, L. J. Wicker, E. R. Mansell, and R. L. Tanamachi, 2012: Impact of the environmental low-level wind profile on ensemble forecasts of the 4 May 2007 Greensburg, Kansas, tornadic storm and associated mesocyclones. *Mon. Wea. Rev.,* **140,** 696–716, doi:10.1175/MWR-D-11-00008.1.

Dowell, D. C., and L. J. Wicker, 2009: Additive noise for storm-scale ensemble forecasting and data assimilation. *J. Atmos. Oceanic Technol.,* **26,** 911–927, doi:10.1175/2008JTECHA1156.1.

——, F. Zhang, L. J. Wicker, C. Snyder, and N. A. Crook, 2004: Wind and temperature retrievals in the 17 May 1981 Arcadia, Oklahoma, supercell: Ensemble Kalman filter experiments. *Mon. Wea. Rev.,* **132,** 1982–2005, doi:10.1175/1520-0493(2004)132<1982:WATRIT>2.0.CO;2.

——, G. Romine, and C. Snyder, 2010: Ensemble storm-scale data assimilation and prediction for severe convective storms. Preprints, *25th Conf. on Severe Local Storms,* Denver, CO, Amer. Meteor. Soc., 9.5. [Available online at https://ams.confex.com/ams/pdfpapers/176121.pdf.]

——, L. J. Wicker, and C. Snyder, 2011: Ensemble Kalman filter assimilation of radar observations of the 8 May 2003 Oklahoma City supercell: Influences of reflectivity observations on storm-scale analyses. *Mon. Wea. Rev.,* **139,** 272–294, doi:10.1175/2010MWR3438.1.

Dudhia, J., 1989: Numerical study of convection observed during the Winter Monsoon Experiment using a mesoscale two-dimensional model. *J. Atmos. Sci.,* **46,** 3077–3107, doi:10.1175/1520-0469(1989)046<3077:NSOCOD>2.0.CO;2.

Edwards, R., A. R. Dean, R. L. Thompson, and B. T. Smith, 2012: Convective modes for significant severe thunderstorms in the contiguous United States. Part III: Tropical cyclone tornadoes. *Wea. Forecasting,* **27,** 1507–1519, doi:10.1175/WAF-D-11-00117.1.

Eilts, M. D., and S. D. Smith, 1990: Efficient dealiasing of Doppler velocities using local environment constraints. *J. Atmos. Oceanic Technol.,* **7,** 118–128, doi:10.1175/1520-0426(1990)007<0118:EDODVU>2.0.CO;2.

Fujita, T., D. J. Stensrud, and D. C. Dowell, 2007: Surface data assimilation using an ensemble Kalman filter approach with initial condition and model physics uncertainty. *Mon. Wea. Rev.,* **135,** 1846–1868, doi:10.1175/MWR3391.1.

Gaspari, G., and S. E. Cohn, 1999: Construction of correlation functions in two and three dimensions. *Quart. J. Roy. Meteor. Soc.,* **125,** 723–757, doi:10.1002/qj.49712555417.

Grell, G. A., and D. Devenyi, 2002: A generalized approach to parameterizing convection combining ensemble and data assimilation techniques. *Geophys. Res. Lett.,* **29,** 1693, doi:10.1029/2002GL015311.

Hong, S.-Y., Y. Noh, and J. Dudhia, 2006: A new vertical diffusion package with an explicit treatment of entrainment processes. *Mon. Wea. Rev.,* **134,** 2318–2341, doi:10.1175/MWR3199.1.

Iacono, M. J., J. S. Delamere, E. J. Mlawer, M. W. Shephard, S. A. Clough, and W. D. Collins, 2008: Radiative forcing by long-lived greenhouse gases: Calculations with the AER radiative transfer models. *J. Geophys. Res.,* **113,** D13103, doi:10.1029/2008JD009944.

Janjić, Z. I., 2002: Nonsingular implementation of the Mellor–Yamada level 2.5 scheme in the NCEP Meso model. NCEP Office Note 437, 61 pp. [Available online at http://www.emc.ncep.noaa.gov/officenotes/newernotes/on437.pdf.]

Jung, Y., M. Xue, and M. Tong, 2012: Ensemble Kalman filter analyses of the 29–30 May 2004 Oklahoma tornadic thunderstorm using one- and two-moment bulk microphysics schemes, with verification against polarimetric radar data. *Mon. Wea. Rev.,* **140,** 1457–1475, doi:10.1175/MWR-D-11-00032.1.

Kain, J. S., 2004: The Kain–Fritsch convective parameterization: An update. *J. Appl. Meteor.,* **43,** 170–181, doi:10.1175/1520-0450(2004)043<0170:TKCPAU>2.0.CO;2.

——, and J. M. Fritsch, 1993: Convective parameterization for mesoscale models: The Kain–Fritsch scheme. *The Representation of Cumulus Convection in Numerical Models, Meteor. Monogr.,* No. 46, Amer. Meteor. Soc., 165–170.

——, and Coauthors, 2008: Some practical considerations regarding horizontal resolution in the first generation of operational convection-allowing NWP. *Wea. Forecasting,* **23,** 931–952, doi:10.1175/WAF2007106.1.

Knupp, K. R., and Coauthors, 2014: Meteorological overview of the devastating 27 April 2011 tornado outbreak. *Bull. Amer. Meteor. Soc.,* **95,** 1041–1062, doi:10.1175/BAMS-D-11-00229.1.

Lakshmanan, V., K. Hondl, G. Stumpf, and T. Smith, 2003: Quality control of WSR-88D data. Preprints, *31st Int. Conf. on Radar Meteorology,* Seattle, WA, Amer. Meteor. Soc., 7B.1. [Available online at https://ams.confex.com/ams/pdfpapers/62597.pdf.]

——, T. Smith, G. Stumpf, and K. Hondl, 2007: The Warning Decision Support System–Integrated Information. *Wea. Forecasting,* **22,** 596–612, doi:10.1175/WAF1009.1.

Lange, H., and G. C. Craig, 2014: The impact of data assimilation length scales on analysis and prediction of convective storms. *Mon. Wea. Rev.,* **142,** 3781–3808, doi:10.1175/MWR-D-13-00304.1.

Liu, Z., C. S. Schwartz, C. Snyder, and S.-Y. Ha, 2012: Impact of assimilating AMSU-A radiances on forecasts of 2008 Atlantic tropical cyclones initialized with a limited-area ensemble Kalman filter. *Mon. Wea. Rev.,* **140,** 4017–4034, doi:10.1175/MWR-D-12-00083.1.

Majcen, M., P. Markowski, Y. Richardson, D. Dowell, and J. Wurman, 2008: Multipass objective analyses of Doppler radar data. *J. Atmos. Oceanic Technol.,* **25,** 1845–1858, doi:10.1175/2008JTECHA1089.1.

Miller, M. L., V. Lakshmanan, and T. Smith, 2013: An automated method for depicting mesocyclone paths and intensities. *Wea. Forecasting,* **28,** 570–585, doi:10.1175/WAF-D-12-00065.1.

Mlawer, E. J., S. J. Taubman, P. D. Brown, M. J. Iacono, and S. A. Clough, 1997: Radiative transfer for inhomogeneous atmospheres: RRTM, a validated correlated-k model for the longwave. *J. Geophys. Res.,* **102,** 16 663–16 682, doi:10.1029/97JD00237.

Nakanishi, M., and H. Niino, 2006: An improved Mellor–Yamada level 3 model: Its numerical stability and application to a regional prediction of advecting fog. *Bound.-Layer Meteor.,* **119,** 397–407, doi:10.1007/s10546-005-9030-8.

——, and ——, 2009: Development of an improved turbulence closure model for the atmospheric boundary layer. *J. Meteor. Soc. Japan,* **87,** 895–912, doi:10.2151/jmsj.87.895.

National Weather Service Birmingham, cited 2014: Historic tornado outbreak—April 27, 2011. [Available online at http://www.srh.noaa.gov/bmx/?n=event_04272011.]

NOAA, 2012: The historic tornadoes of April 2011. NWS Service Assessment, 76 pp. [Available online at www.nws.noaa.gov/os/assessments/pdfs/historic_tornadoes.pdf.]

Potvin, C. K., and L. J. Wicker, 2013: Assessing ensemble forecasts of low-level supercell rotation within an OSSE framework. *Wea. Forecasting,* **28,** 940–960, doi:10.1175/WAF-D-12-00122.1.

Putnam, B. J., M. Xue, Y. Jung, N. A. Snook, and G. Zhang, 2014: The analysis and prediction of microphysical states and polarimetric variables in a mesoscale convective system using double-moment microphysics, multinetwork radar data, and the ensemble Kalman filter. *Mon. Wea. Rev.,* **142,** 141–162, doi:10.1175/MWR-D-13-00042.1.

Romine, G. S., C. S. Schwartz, C. Snyder, J. L. Anderson, and M. L. Weisman, 2013: Model bias in a continuously cycled assimilation system and its influence on convection-permitting forecasts. *Mon. Wea. Rev.,* **141,** 1263–1284, doi:10.1175/MWR-D-12-00112.1.

Schumacher, R. S., and A. J. Clark, 2014: Evaluation of ensemble configurations for the analysis and prediction of heavy-rain-producing mesoscale convective systems. *Mon. Wea. Rev.,* **142,** 4108–4138, doi:10.1175/MWR-D-13-00357.1.

Schwartz, C. S., and Coauthors, 2010: Toward improved convection-allowing ensembles: Model physics sensitivities and optimizing probabilistic guidance with small ensemble membership. *Wea. Forecasting,* **25,** 263–280, doi:10.1175/2009WAF2222267.1.

——, G. S. Romine, K. R. Smith, and M. L. Weisman, 2014: Characterizing and optimizing precipitation forecasts from a convection-permitting ensemble initialized by a mesoscale ensemble Kalman filter. *Wea. Forecasting,* **29,** 1295–1318, doi:10.1175/WAF-D-13-00145.1.

Skamarock, W. C., and Coauthors, 2008: A description of the Advanced Research WRF version 3. NCAR Tech. Note NCAR/TN-475+STR, 113 pp. [Available online at http://www2.mmm.ucar.edu/wrf/users/docs/arw_v3.pdf.]

Snook, N., M. Xue, and J. Jung, 2011: Analysis of a tornadic mesoscale convective vortex based on ensemble Kalman filter assimilation of CASA X-band and WSR-88D radar data. *Mon. Wea. Rev.,* **139,** 3446–3468, doi:10.1175/MWR-D-10-05053.1.

——, ——, and ——, 2012: Ensemble probabilistic forecasts of a tornadic mesoscale convective system from ensemble Kalman filter analyses using WSR-88D and CASA radar data. *Mon. Wea. Rev.,* **140,** 2126–2146, doi:10.1175/MWR-D-11-00117.1.

Snyder, C., and F. Zhang, 2003: Assimilation of simulated Doppler radar observations with an ensemble Kalman filter. *Mon. Wea. Rev.,* **131,** 1663–1677, doi:10.1175//2555.1.

Stensrud, D. J., and J. Gao, 2010: Importance of horizontally inhomogeneous environmental initial conditions to ensemble storm-scale radar data assimilation and very short-range forecasts. *Mon. Wea. Rev.,* **138,** 1250–1272, doi:10.1175/2009MWR3027.1.

——, J.-W. Bao, and T. T. Warner, 2000: Using initial condition and model physics perturbations in short-range ensemble simulations of mesoscale convective systems. *Mon. Wea. Rev.,* **128,** 2077–2107, doi:10.1175/1520-0493(2000)128<2077:UICAMP>2.0.CO;2.

——, and Coauthors, 2009a: Convective-scale warn-on-forecast system: A vision for 2020. *Bull. Amer. Meteor. Soc.,* **90,** 1487–1499, doi:10.1175/2009BAMS2795.1.

——, N. Yussouf, D. C. Dowell, and M. C. Coniglio, 2009b: Assimilating surface data into a mesoscale model ensemble: Cold pool analyses from spring 2007. *Atmos. Res.,* **93,** 207–220, doi:10.1016/j.atmosres.2008.10.009.

——, and Coauthors, 2013: Progress and challenges with Warn-on-Forecast. *Atmos. Res.,* **123,** 2–16, doi:10.1016/j.atmosres.2012.04.004.

Sun, J., and N. A. Crook, 2001: Real-time low-level wind and temperature analysis using single WSR-88D data. *Wea. Forecasting,* **16,** 117–132, doi:10.1175/1520-0434(2001)016<0117:RTLLWA>2.0.CO;2.

Tewari, M., and Coauthors, 2004: Implementation and verification of the unified NOAH land surface model in the WRF model. Preprints, *20th Conf. on Weather Analysis and Forecasting/16th Conf. on Numerical Weather Prediction,* Seattle, WA, Amer. Meteor. Soc., 14A.2. [Available online at https://ams.confex.com/ams/pdfpapers/69061.pdf.]

Thompson, G., R. M. Rasmussen, and K. Manning, 2004: Explicit forecasts of winter precipitation using an improved bulk microphysics scheme. Part I: Description and sensitivity analysis. *Mon. Wea. Rev.,* **132,** 519–542, doi:10.1175/1520-0493(2004)132<0519:EFOWPU>2.0.CO;2.

——, P. R. Field, W. R. Hall, and R. M. Rasmussen, 2008: Explicit forecasts of winter precipitation using an improved bulk microphysics scheme. Part II: Implementation of a new snow parameterization. *Mon. Wea. Rev.,* **136,** 5095–5115, doi:10.1175/2008MWR2387.1.

Thompson, R. L., B. Smith, J. S. Grams, A. R. Dean, and C. Broyles, 2012: Convective modes for significant severe thunderstorms in the contiguous United States. Part II: Supercell and QLCS tornado environments. *Wea. Forecasting,* **27,** 1136–1154, doi:10.1175/WAF-D-11-00116.1.

Tiedtke, M., 1989: A comprehensive mass flux scheme for cumulus parameterization in large-scale models. *Mon. Wea. Rev.,* **117,** 1779–1800, doi:10.1175/1520-0493(1989)117<1779:ACMFSF>2.0.CO;2.

Tong, M., and M. Xue, 2005: Ensemble Kalman filter assimilation of Doppler radar data with a compressible nonhydrostatic model: OSS experiments. *Mon. Wea. Rev.,* **133,** 1789–1807, doi:10.1175/MWR2898.1.

Toth, Z., Y. Zhu, and R. Wobus, 2004: March 2004 upgrades of the NCEP global ensemble forecast system. NOAA/NCEP/EMC. Accessed 2014. [Available online at http://www.emc.ncep.noaa.gov/gmb/ens/ens_imp_news.html.]

TRAC, 2012: Cultivating a state of readiness: Our response to April 27, 2011. Tornado Recovery Action Council (TRAC) of Alabama, 117 pp. [Available online at http://tracAL.org/wp-content/uploads/2012/01/TRAC_Report.pdf.]

Trapp, R. J., E. D. Robinson, M. E. Baldwin, N. S. Diffenbaugh, and B. R. J. Schwedler, 2011: Regional climate of hazardous convective weather through high-resolution dynamical downscaling. *Climate Dyn.,* **37,** 677–688, doi:10.1007/s00382-010-0826-y.

Wei, M., Z. Toth, R. Wobus, and Y. Zhu, 2008: Initial perturbations based on the ensemble transform (ET) technique in the NCEP global operational forecast system. *Tellus,* **60A,** 62–79, doi:10.1111/j.1600-0870.2007.00273.x.

Wheatley, D. M., D. J. Stensrud, D. C. Dowell, and N. Yussouf, 2012: Application of a WRF mesoscale data assimilation system to springtime severe weather events 2007–09. *Mon. Wea. Rev.,* **140,** 1539–1557, doi:10.1175/MWR-D-11-00106.1.

——, N. Yussouf, and D. J. Stensrud, 2014: Ensemble Kalman filter analyses and forecasts of a severe mesoscale convective system using different choices of microphysics schemes. *Mon. Wea. Rev.,* **142,** 3243–3263, doi:10.1175/MWR-D-13-00260.1.

Xue, M., K. K. Droegemeier, and V. Wong, 2000: The Advanced Regional Prediction System (ARPS)—A multiscale nonhydrostatic atmospheric simulation and prediction tool. Part I: Model dynamics and verification. *Meteor. Atmos. Phys.,* **75,** 161–193, doi:10.1007/s007030070003.

——, M. Tong, and K. K. Droegemeier, 2006: An OSSE framework based on the ensemble square root Kalman filter for evaluating the impact of data from radar networks on thunderstorm analysis and forecasting. *J. Atmos. Oceanic Technol.,* **23,** 46–66, doi:10.1175/JTECH1835.1.

Yussouf, N., and D. J. Stensrud, 2010: Impact of phased-array radar observations over a short assimilation period: Observing system simulation experiments using an ensemble Kalman filter. *Mon. Wea. Rev.,* **138,** 517–538, doi:10.1175/2009MWR2925.1.

——, and ——, 2012: Comparison of single-parameter and multiparameter ensembles for assimilation of radar observations using the ensemble Kalman filter. *Mon. Wea. Rev.,* **140,** 562–586, doi:10.1175/MWR-D-10-05074.1.

——, J. Gao, D. J. Stensrud, and G. Ge, 2013a: The impact of mesoscale environmental uncertainty on the prediction of a tornadic supercell storm using ensemble data assimilation approach. *Adv. Meteor.,* **2013,** 1–15, doi:10.1155/2013/731647.

——, E. R. Mansell, L. J. Wicker, D. M. Wheatley, and D. J. Stensrud, 2013b: The ensemble Kalman filter analyses and forecasts of the 8 May 2003 Oklahoma City tornadic supercell storm using single- and double-moment microphysics schemes. *Mon. Wea. Rev.,* **141,** 3388–3412, doi:10.1175/MWR-D-12-00237.1.

Zhang, C., Y. Wang, and K. Hamilton, 2011b: Improved representation of boundary layer clouds over the southeast Pacific in ARW-WRF using a modified Tiedtke cumulus parameterization scheme. *Mon. Wea. Rev.,* **139,** 3489–3513, doi:10.1175/MWR-D-10-05091.1.

Zhang, J., and Coauthors, 2011a: National Mosaic and Multi-Sensor QPE (NMQ) system: Description, results, and future plans. *Bull. Amer. Meteor. Soc.,* **92,** 1321–1338, doi:10.1175/2011BAMS-D-11-00047.1.

Ziegler, C. L., E. R. Mansell, J. M. Straka, D. R. MacGorman, and D. W. Burgess, 2010: The impact of spatial variations of low-level stability on the life cycle of a simulated supercell storm. *Mon. Wea. Rev.,* **138,** 1738–1766, doi:10.1175/2009MWR3010.1.